THE ASTROPHYSICAL JOURNAL, 460:801–826, 1996 April 1

THE DYNAMICS AND OUTCOMES OF RAPID INFALL ONTO NEUTRON STARS

CHRIS L. FRYER AND WILLY BENZ
Steward Observatory, University of Arizona, Tucson, AZ 85721; cfryer@as.arizona.edu

AND

MARC HERANT
Theory Division, MS K710, Los Alamos National Laboratory, Los Alamos, NM 87545
Received 1995 May 12; accepted 1995 September 25

ABSTRACT

We present an extensive study of accretion onto neutron stars in which the velocity of the neutron star and structure of the surrounding medium is such that the Bondi-Hoyle accretion exceeds $10^{-4}\ M_\odot$ yr^{-1}. Two types of initial conditions are considered for a range of entropies and chemical compositions: an atmosphere in pressure equilibrium above the neutron star, and a freely falling inflow of matter from infinity (also parameterized by the infall rate). We then evolve the system with one- and two-dimensional hydrodynamic codes to determine the outcome. For most cases, hypercritical (also termed "super Eddington") accretion caused by rapid neutrino cooling allows the neutron star to accrete above the Bondi-Hoyle rate as previously pointed out by Chevalier. However, for a subset of simulations which corresponds to evolutionarily common events, convection driven by neutrino heating can lead to explosions by a mechanism similar to that found in core-collapse supernovae.

Armed with the results from our calculations, we are in a position to predict the fate of a range of rapid-infall neutron star accretors present in certain low-mass X-ray binaries, common envelope systems, supernova fallbacks, and Thorne-Zytkow objects (TZOs). A majority of the common envelope systems that we considered led to explosions expelling the envelope, halting the neutron star's inward spiral, and allowing the formation of close binary systems. As a result, the smothered neutron stars produced in the collisions studied by Davies & Benz may also explode, probably preventing them from forming millisecond pulsars. For the most massive supernovae, in which the fallback of material toward the neutron star after a successful explosion is large, we find that a black hole is formed in a few seconds. Finally, we argue that the current set of TZO formation scenarios is inadequate and leads instead to hypercritical accretion and black hole formation. Moreover, it appears that many of the current TZ models have structures ill suited for modeling by mixing-length convection. This has prompted us to develop a simple test to determine the viability of this approximation for a variety of convective systems.

Subject headings: accretion, accretion disks — binaries: close — hydrodynamics — stars: neutron

1. INTRODUCTION

It is only in the last few decades, with the arrival of high-energy observatories, that the problem of accretion onto neutron stars has moved from the speculations of theorists to the constraints of observations. Satellites such as *Einstein*, *ROSAT*, *GRO*, *Ginga*, and others have contributed to a growing list of accreting neutron star sources such as gamma-ray bursters, X-ray bursters, millisecond pulsars, high-mass X-ray binaries (HMXBs), low-mass X-ray binaries (LMXBs), and a number of objects entangled within the current evolutionary scenarios for binary pulsars. Future observations (*AXAF*, *NAE*, etc.) promise to add more. Unfortunately, the current state of theoretical models falls short of the present and upcoming data. At the root of the theoretical difficulties is the range of extreme physical conditions encountered in many of the observed systems: high magnetic fields, angular momentum, degenerate matter, neutrino effects, etc. In addition, as we shall demonstrate in this paper, it is likely that multidimensional effects are important. As a result, progress in understanding neutron star accretion has been slow. In this paper, the first of a series, we will consider the effects of rapid mass infall onto neutron stars ($\dot{M}_{\text{Bondi-Hoyle}} > 10^{-3}\ M_\odot\ \mathrm{yr}^{-1}$. By *infall* rate, we mean the rate at which material is added to the atmosphere surrounding the neutron star. This is to be distinguished from the term *accretion*, which we reserve for the mass incorporated into the neutron star. High infall rates occur in common envelope systems such as Be/X-ray objects, more deeply buried systems such as Thorne-Zytkow objects (TZOs), and supernova fallback.

Early work studying rapid mass infall onto neutron stars logically began with estimates of the fallback of matter onto newborn neutron stars in supernovae (Colgate 1971; Zeldovich, Ivanova, & Nadezhin 1972). Both groups found that the canonical photon Eddington accretion rate vastly underestimates accretion onto the neutron star as neutrino rather than photon, emission becomes the dominant cooling source. Chevalier (1989) and Houck & Chevalier (1991) have studied in greater analytic detail the fallback of matter onto the adolescent neutron star, confirming this "hypercritical" accretion rate. Even though the amount of fallback matter is generally a small fraction of the material expelled by the supernova, it is a large portion of the material undergoing heavy element nucleosynthesis. Thus, understanding supernova fallback is crucial, not only to decide whether or not a neutron star or black hole is left after the explosion, but also to understand the nucleosynthetic yields of supernova explosions which, in turn, have profound repercussions for galactic chemical evolution.

However, most of the interest in atmospheres around neutron stars has been directed toward understanding Thorne-Zytkow objects, a hypothetical red giant in which

the normally white dwarf–like core is a neutron star. These objects are supported, in addition to the "normal" contribution from thermonuclear burning, by the release of gravitational energy from accretion onto the neutron star, and therefore they have longer lifetimes than standard red giants. The concept of powering a star from mass accretion onto a degenerate object was revived from its pre-fusion days (Landau 1937) by Thorne and Zytkow (1975). In their study of a range of models for stellar envelopes greater than 1 $M_\odot$, Thorne & Zytkow (1977) separated their models into two classes depending upon atmosphere mass. For the more massive envelopes, accretion alone is insufficient to provide pressure support, suggesting nuclear burning arising from the extreme conditions near the surface of the neutron star as a possible complementary mechanism. Follow-up work by Biehle (1991, 1994), Cannon et al. (1992), and Cannon (1993) focused on this class of objects, using more detailed descriptions of the nuclear burning. These simulations established abnormal nuclear burning (such as the *rp*-process) as an additional source of pressure support and led to more definitive results on the observable chemical compositions of TZOs, should they exist. In recent years, the usage of the term TZO has grown in the literature to encompass a broader range of neutron star atmosphere systems. In this paper, we reserve the TZO designation for those objects originally envisioned by Thorne & Zytkow and the other authors listed in this paragraph.

As an ever-branching list of formation scenarios has been dreamed up, the occurrence of rapid infall on neutron stars has evolved from the seed of a theorist's imagination to a virtual certainty. Among them, one finds (1) supernova fallback, (2) common envelope evolution (Taam, Bodenheimer, & Ostriker 1978; Terman, Taam, & Hernquist 1994), (3) collisions between main-sequence stars or red giants and neutron stars in globular clusters or galactic nuclei (Benz & Hills 1992; Davies & Benz 1995), (4) an induced collision between a newly formed neutron star and its binary companion as it is kicked by an asymmetric supernova explosion (Leonard, Hills, & Dewey 1994), and (5) a neutron star caught within the torus of an active galactic nucleus or within a dense molecular cloud (D. N. C. Lin, private communication). Supernova fallback excepted, not much attention has been paid to the link between formation scenario and their hypothetical product (LMXBs, TZOs, etc.). Along those lines, the stability of the buildup of an atmosphere around a neutron star has been in dispute ever since TZ objects were conjectured. At the heart of this controversy is the impact of neutrino physics on the structure of the atmosphere. Neutrino cooling, an aspect of the problem first brought up by Bisnovatyi-Kogan & Lamzin (1984), dismissed by Eich et al. (1989), and subsequently ignored by Biehle (1991, 1994), Cannon et al. (1992), and Cannon (1993), has regained prominence as understanding of supernova fallback onto neutron stars has progressed. In particular, Chevalier (1993) has found that hypercritical accretion can occur, not only in the case of supernova fallback, but also in the entire range of common envelope systems, including TZ objects.

This paper is about what occurs when a neutron star is forced to accrete matter at a high rate. A generic scenario might be as follows: a neutron star encounters a star (or a gas cloud, or an active galactic nucleus [AGN] disk, or its own ejecta). During an initial transient, an accretion shock moves from the surface of the neutron star to some equilibrium radius. The region inside the shock then becomes an atmosphere in near-pressure equilibrium which settles on the neutron star. Both of these phases of the evolution can last for many dynamical times so that it is not possible to model the comprehensive evolution of the accreting neutron star. Since we would still like to determine what the final outcome will be, we have decided the following plan of attack: in a first set of simulations, we compute the evolution of a series of initial free-fall conditions over a range of parameters (entropy, chemical composition, and most importantly, infall rate). These conditions typify the expected initial structure obtained as a neutron star plows into a medium. For reasons explained in § 4.1.1, the transient structure which develops while the accretion shock moves outward immediately becomes convectively unstable, pushing the accretion shock beyond its steady state radius. Unfortunately, the convective episode lasts too long to follow to completion, but the end result can be inferred, namely, that an isentropic atmosphere will eventually build up above the neutron star. In a second set of simulations, we examine just such isentropic atmospheres initially in gravitational and pressure equilibrium for a range of entropy and chemical composition. In the absence of neutrino processes, these atmospheres are stable. Starting with these "pseudo-stable" initial conditions, we turn on neutrino processes and determine how stability is affected by energy losses due to neutrino emission. Combining these two sets of simulations, we can take a given infall structure and, using our first set of models, estimate the resulting structure of the isentropic atmosphere. With this structure, the second series of models will then predict the ultimate fate of the system.

Section 2 discusses the numerical methods used in our simulations, and § 3 presents the range of initial conditions and physical processes included in this study. The results, including comparisons to the work of Chevalier (1989, hereafter C89), Chevalier (1993), Houck & Chevalier (1991), hereafter HC), and Colgate, Herant, & Benz (1993, hereafter CHB), are presented in § 4. We conclude with a discussion of the implications of our findings for the variety of systems involving high-mass infall and the potential observational consequences.

2. NUMERICAL METHODS

To explore the behavior of our range of atmospheres, we utilize both one-dimensional and two-dimensional codes. The one-dimensional code is used to determine the subset of atmospheres that develop negative entropy gradients of sufficient magnitudes to induce convection and thus break the otherwise spherical symmetry. This allows us to limit multidimensional simulations to those atmospheres that really require it. All physical processes such as neutrino physics (absorption, emission and transport), equation of state, etc., are implemented in identical ways for both codes. The two codes have already been described in detail (Herant et al. 1994, hereafter HBHFC). Thus, we will limit ourselves to an overview except to describe modifications introduced specifically for these simulations.

2.1. *One-dimensional Lagrangian Code*

The one-dimensional simulations were performed with an explicit, grid-based, Lagrangian code (Benz 1991) using a second-order Runge-Kutta integrator. This code does not include any form of convection modeling (mixing-length or

other), and as a result, its usefulness is limited to nonconvective regimes and to the diagnosis of the onset of convection. The neutron star surface is modeled by a reflective inner boundary, exterior to which lies the atmosphere. For most of the one-dimensional simulations, we used a total of 140 cells modeling the pressure equilibrium atmospheres out to a radius $\sim$2500 km and the infall atmospheres out to $\sim$25,000 km. Since the mass of the atmosphere depends strongly on entropy for the equilibrium models (see eq. [39]) and on the infall rate for the infall models (see eq. [13]), the mass resolution for the models varies according to the computed model. However, it was chosen in such a way as to maximize resolution near the surface of the neutron star.

Both Newtonian and general relativistic (in the style of Van Riper 1979) formalisms have been implemented in the code. We have found that the general relativistic implementation leads to an increase in the Brunt-Väisälä frequency of up to 40% over the Newtonian case in the intermediate entropy models (see § 4.2.2), and in addition, a factor of $\sim$3 increase in accretion rates. These effects are comparable to those calculated by HC. However, since angular momentum and accretion concerns limit us to mostly qualitative estimates anyway, in most of the simulations presented here, general relativistic effects have been ignored.

2.2. *Two-dimensional SPH Code*

The basic structure of the two-dimensional cylindrical geometry smooth particle hydrodynamics (SPH) code used for the simulations of this paper has been presented in Herant & Benz (1992). The code was developed further in Herant, Benz, & Colgate (1992) and HBHFC to incorporate neutrino processes and an equation of state of extended range.

As in HBHFC, we run our calculations in a wedge centered on the equatorial plane with periodic boundary conditions to avoid the complications associated with the z-axis which corresponds to a singularity of the cylindrical coordinate system. The opening angle is usually 90°, corresponding to $(2)^{1/2}/2$ of the total volume. We have varied the opening angle (up to 160°) and the number of particles (factors of 4 [4000–16,000 particles]) in the simulations without noticing appreciable changes in the results. The gravitational force is calculated in the Newtonian limit by evaluating the mass interior to each particle, thereby assuming spherical symmetry, which is reasonable considering that the central neutron star provides the dominant contribution. The kernel used is the same as in HBHFC.

The structure of the initial atmospheres (see § 3.1) is mapped to an SPH representation. Particles are placed on concentric circles around the origin. There are of order 50 particles per circle, which in a 90° wedge translates to an angular resolution of few degrees. As in the one-dimensional case, the mass of the particles is dependent upon the specific characteristics of the atmosphere being studied with the maximal mass resolution near the surface of the neutron star. Also similar to the one-dimensional code, a fixed, hard boundary represents the neutron star surface. Its implementation is as described in HBHFC. Once particles reach a critical density ($\rho > 10^{13}$ g cm^{-3}) and electron fraction ($Y_e < 0.1$), they are accreted onto the neutron star surface. In addition, an outer boundary was introduced to allow us to control the pressure of the outer atmosphere.

3. INITIAL CONDITIONS AND PHYSICAL PROCESSES

3.1. *Initial Conditions*

In most of our simulations, the neutron star has a 1.4 $M_\odot$ gravitational mass and a radius of 10 km. Atmospheres with initially uniform entropy and chemical composition are constructed above the neutron star. Their initial density structure is determined by pressure equilibrium in the equilibrium atmosphere models, or by assigning a mass infall rate and assuming free-fall initial conditions for the infall simulations. We considered initial compositions of pure iron, pure oxygen, and a primordial mix of hydrogen and helium. Because the temperature at the base of the atmosphere is usually high enough to lead to nuclear statistical equilibrium (NSE), the initial composition is important to determine the energy release from nuclear burning.

For the equilibrium atmosphere calculations, pressure equilibrium was verified in our code by allowing the atmosphere to evolve hydrodynamically without neutrino physics. For the two-dimensional simulations, inaccuracies in the mapping scheme from the one-dimensional structure lead to small initial transients which have to be damped, preserving constancy of entropy. In general, however, the atmospheres were found to remain in equilibrium for times much longer than our simulation times.

3.2. *Equation of State and Neutrino Processes*

The equation of state and neutrino processes are discussed in HBHFC, to which the reader is referred for further details. The equation of state includes perfect gas, photon, and electron contributions to any degree of degeneracy and relativism (Nadezhin 1974; Blinnikov, Dunina-Barkovskaya, & Nadezhin 1995), and a nuclear equation of state (Lattimer & Swesty 1991). In addition, when the temperature rises above 5×10^9 K, NSE (see Hix et al. 1995) is enforced to approximate the effect of nuclear burning and to compute the free nucleon fraction which is important for neutrino emission and absorption. Although matter does burn at lower temperatures without going immediately into NSE, burning is a slow process compared to the hydrodynamics.

The neutrino emission processes accounted for include electron and positron capture by free protons and neutrons, and pair and plasma neutrino-antineutrino creation. Neutrino absorption processes include electron neutrino capture by free neutrons, electro antineutrino by free protons, and neutrino antineutrino annihilation. Neutrino scattering includes electron and positron scattering of neutrinos and neutral current opacities by nuclei. Three species of neutrinos are tracked separately by the transport algorithm: electron neutrino, electron antineutrino, and a generic "τ" neutrino bundling together μ and τ neutrino and antineutrinos which have very similar characteristics in the regimes under consideration. The neutrino transport consists of two schemes: flux-limited diffusion for the optically thick regions and a light-bulb approximation for the optically thin regions. The light-bulb approximation was introduced for computational speed and is only valid if the absorbed neutrino luminosity ($L_{\nu_{abs}}$) in this regime is much less than the total neutrino luminosity ($L_{\nu_{tot}}$). In most of our calculations, we limit the $L_{\nu_{abs}}/L_{\nu_{tot}}$ to 10%. We have run test calculations limiting $L_{\nu_{abs}}/L_{\nu_{tot}}$ to 3% without appreciable changes in the results.

3.3. *Infall Rates and Assumptions*

The objective of this paper is to determine the effect of neutrino processes on accretion for a range of initial conditions. We then apply our results to specific circumstances which lead to rapid infall on neutron stars. In this section we discuss the probable infall rates for various scenarios and the suitability of our assumptions, which include ignoring the effects of angular momentum, magnetic fields, and photon diffusion.

3.3.1. *Infall*

The infall of matter onto a neutron star plowing through a medium is characterized for many, if not all, of the formation scenarios by Bondi-Hoyle "infall" and has been studied further numerically in a series of papers by Ruffert (1994a, b, 1995) and Ruffert & Arnett (1994). They compare numerical results to the canonical Bondi-Hoyle infall in a homogeneous medium and introduce a new set of equations to estimate the infall rate. However, except at Mach numbers (M) close to 1, the infall rate is within 20% of the canonical rate (it can increase by factors of 3 for $M = 1$ infall). Since we are only interested in rough estimates of the infall, we will use the simpler equations of Bondi-Hoyle-Lyttleton (Bondi 1952):

$$\dot{M}_{\rm B} \approx 4\pi r_{\rm B}^2 \rho (v^2 + c_s^2)^{1/2} , \tag{1}$$

where the Bondi infall radius is

$$r_{\rm B} = \frac{GM_{\rm NS}}{v^2 + c_s^2} , \tag{2}$$

G is the gravitational constant, and ρ and c_s are the density and sound speed of the ambient medium. Table 1 lists the infall radii and infall rates for a neutron star plowing through stars (modeled with a stellar structure code developed by D. Arnett) of different masses and at different distances from the center for a range of impact velocities spanning possible high infall scenarios. Note that proper-motion measurements of neutron stars imply an average spatial velocity of neutron stars on the order of 450 km s^{-1} and, in some cases, as high as 1000 km s^{-1} (Lyne & Lorimer 1994; Frail, Gross, & Whiteoak 1994). However, common envelope systems will involve much lower velocities ($\sim v_{\rm orbital}$).

3.3.2. *Angular Momentum*

Estimating the effects of inhomogeneous media on Bondi-Hoyle accretion has been fraught with difficulties both from an analytic and numeric standpoint. Analytical approaches tend to depend heavily upon unphysical assumptions (sometimes assuming that the fluid flow system is identical to the standard Bondi-Hoyle structure for the homogeneous case), and in general, results have not been corroborated by simulations. Moreover, the lack of agreement among numerical endeavors has made their estimates equally inconclusive. A partial list of numerical studies representing the large variation in results includes Davies & Pringle (1980), Fryxell & Taam (1988), Taam & Fryxell (1989), Sawada et al. (1989), Theuns & Jorissen (1993), and Ruffert & Anzer (1995). Most of these discrepancies are probably due to differences in resolution, boundary effects, or a difference in accretion between two- and three-dimensional models. However, the numerical simulations virtually all agree on two points: the average infall rate is within a factor of 2 of the Bondi-Hoyle infall (even though in many simulations the infall rate is seen to vary with time, e.g., the "flip-flop" instability seen by Fryxell and Taam), and the angular momentum accreted within the accretor radius (typically $0.1 r_{\rm B}$) is generally nonzero, but less than that predicted by a majority of the analytical estimates.

Despite these difficulties, we would like to try to evaluate, using currently favored numerical models, the effects of angular momentum on accretion. A typical estimation for angular momentum accretion is (see, for example, Ruffert & Anzer 1994)

$$j_z \equiv \dot{J}_z/\dot{M} = \tfrac{1}{4}(6\epsilon_v - \epsilon_\rho) V r_{\rm B} , \tag{3}$$

where $\dot{J}_z$ is the angular momentum accretion rate, $\dot{M}$ is the mass accretion rate, and V is the velocity of the accretor, and $\epsilon_{v,\rho}$ are the inhomogeneity parameters defined as (Taam & Fryxell 1989)

$$\epsilon_{\rho,v} = r_{\rm B}/H_{\rho,v} , \tag{4}$$

where $H_{\rho,v}$ is the scale height of the density (ρ) or the velocity [including the sound speed, i.e., $(c_s^2 + v^2)^{1/2}$] profile perpendicular to the direction of motion of the accretor. Ruffert & Anzer consider a $V = 3c_s$ accretor in an $\epsilon_v = 0.3$ medium with an accretion radius one-tenth the size of the Bondi radius. Their results give a 40% decrease in the angular momentum accreted in comparison to equation (3). Assuming no angular momentum is lost once the material passes within the accretion radius and using equation (3), one can determine an upper limit for the radius at which rotational support stops the infall ($r_{\rm ang}$) of material (also shown in Table 1). This is most likely an overestimate since, until an axysymmetric regime is attained, angular momentum can be transported effectively by pressure waves and shocks.

From $r_{\rm ang}$ inward, a thick accretion disk forms. For a thick α disk, the timescale for the outward transport of angular momentum is estimated to be (Chevalier 1993)

$$t_{\rm in} \sim \frac{r_{\rm ang}^2}{\alpha c_s H} \sim \frac{r_{\rm ang}^{3/2}}{\alpha\sqrt{GM}} \sim r_8^{1.5} \text{ s} , \tag{5}$$

where the sound speed (c_s) is approximated as the orbital velocity, H is the disk scale height and is estimated to be $\sim r$, α is a measure of the viscous stress typically found to be $\sim$0.01–0.1 (we use 0.07), and r_8 is $r_{\rm ang}$ in units of 10^8 cm. Once the material loses its angular momentum, it will accrete onto the neutron star. Thus, $t_{\rm in}$ is essentially the time delay for the accretion of material. Since $t_{\rm in}$ is not much larger than the free-fall timescale, this delay should have a relatively small impact on the accretion rate.

Despite this discussion, we are aware that the question of the effect of angular momentum accretion is unsettled, and it will remain so until more comprehensive results from numerical and analytical calculations become available. However, we believe that in the case of buried neutron stars, the effect of angular momentum should be a perturbation on the classical Bondi regime. One reason is that the dynamics of the self-gravitating, thick accretion disk is ripe with hydrodynamical instabilities (unlike cold, thin disks), which should allow rapid transport of angular momentum. Another reason for sustained accretion is that just as there exists a plane in which the angular momentum accreted is maximal, there is also a plane in which it is nil, and that is where the accreted matter may come from primarily (i.e.,

1996ApJ...460..801F

TABLE 1

ACCRETION PARAMETERS

Stellar Type	$r_{NS} - r_{SC}$[a] (10^{11} cm)	Density (g cm^{-3})	Entropy (k_B nucleon^{-1})	Velocity (km s^{-1})	c_s (km s^{-1})	Bondi Radius (10^{11} cm)	$\dot{M}$ ($M_\odot$ yr^{-1})	Inhom. Factor $\epsilon_{\rho,v}$	R_{ang} (10^8 cm)	Trap. Radius (10^{11} cm)	Result[b]
1 $M_\odot$ MS	0.4	0.4	15	300	300	1	N/A	N/A	N/A	N/A	N/A
	0.4	0.4	15	100	300	2	N/A	N/A	N/A	N/A	N/A
	0.125	60	12	300	475	0.6	N/A	N/A	N/A	N/A	N/A
	0.125	60	12	100	475	0.8	N/A	N/A	N/A	N/A	N/A
5 $M_\odot$ MS	1.0	0.25	17	300	400	0.75	1.4×10^4	3.4, -0.004	200	0.75	IC
	1.0	0.25	17	100	400	1.0	2.0×10^4	4.5, ~ 0	68	1.0	IC
	0.4	6.3	15	300	550	0.5	2.0×10^5	2.0, -0.20	4.8	0.5	IC
	0.4	6.3	15	100	550	0.6	2.5×10^5	2.4, -0.20	1.2	0.6	IC
10 $M_\odot$ MS	2.0	0.25	18	300	350	0.9	1.8×10^4	2.0, -0.16	26	0.9	IC
	2.0	0.25	18	100	350	1.4	3.5×10^4	3.2, -0.10	44	1.4	IC
	0.6	2.5	17	300	600	0.4	5.0×10^4	1.0, -0.05	2.4	0.4	IC
	0.6	2.5	17	100	600	0.5	7.5×10^4	1.25, -0.06	4.5	0.5	IC
20 $M_\odot$ MS	10.	3×10^{-3}	22	300	200	1.4	300	1.0, 0.07	120	1.4	EX
	10.	3×10^{-3}	22	100	200	4.0	2000	3.0, 0.11	720	4.0	IC
	5.0	0.013	21	300	300	0.74	570	0.3, -0.01	0.10	0.74	EX
	5.0	0.013	21	100	300	1.3	1300	0.52, -0.03	0.06	1.3	IC
10 $M_\odot$ Giant.....	250	5×10^{-8}	26	300	40	2.0	0.01	0.024, ~ 0	0.07	2.0	DC
	250	5×10^{-8}	26	70	40	30	0.7	0.36, -0.01	130	30	EX
	60	3×10^{-7}	26	300	60	2.0	0.06	0.05, -0.01	0.01	2.0	EX
	60	3×10^{-7}	26	70	60	20	2	0.5, -0.05	26	20	EX
	1.0	0.08	10	300	300	0.74	3700	0.58, -0.15	1.7	0.74	IC
	1.0	0.08	10	70	300	2.0	2×10^4	1.6, -0.37	2.5	2.0	IC
20 $M_\odot$ Giant.....	10.	10^{-3}	29	300	250	1.2	100	0.42, 0.07	31	1.2	EX
	10.	10^{-3}	29	100	250	1.8	175	0.63, 0.12	20	1.8	EX
	4.0	0.01	24	300	400	0.5	250	0.25, -0.06	0.09	0.5	EX
	4.0	0.01	24	100	400	1.0	800	0.5, -0.1	0.01	1.0	EX
	0.5	250	10	300	1000	0.17	1.5×10^6	0.20, -0.06	0.02	0.17	IC
	0.5	250	10	100	1000	0.18	1.8×10^6	0.21, -0.07	5×10^{-3}	0.18	IC
GMC	N/A	10^{-11}	45	1000	10	0.2	8×10^{-8}	0?	0?	3×10^{-5}	?
	N/A	10^{-11}	45	300	10	2.0	2×10^{-6}	0?	0?	7×10^{-4}	?
	N/A	10^{-11}	45	10	10	930	0.024	0?	0?	9	?

[a] This is the distance the neutron star is from the center of its companion.

[b] IC = immediate collapse, EX = explosion, DC = delayed collapse.

the polar direction in the case of an inspiral). Since the submission of this paper, Chevalier (1995) has submitted a paper which discusses in detail the problems and concerns surrounding angular momentum.

3.3.3. *Photon Diffusion*

Our current set of simulations is limited by the assumption that the photons are "trapped" within the material of the atmospheres. By trapped, we mean that the photons are carried inward with the accretion flow significantly faster than the speed at which they can diffuse outward. As a result, we only consider cases for which the accretion rate is sufficiently high (infall models), or for which the entropy is not too large (equilibrium atmosphere models). We derive below the conditions for which the assumption of photon trapping is valid.

For equilibrium atmospheres, the timescales for neutrino cooling (τ_ν) sets the accretion rate and therefore the dynamical timescale. Therefore, we can compare the photon diffusion timescale (τ_γ, calculated near the surface of the neutron star since this is where the interesting dynamics occur) with τ_ν to determine the range of constant-entropy, equilibrium atmospheres for which we can assume neutrinos are trapped. Using the approximations for the structure of the equilibrium atmospheres derived in § 4.2, we obtain

$$\tau_\nu = E_{\rm reg}/L_{\rm reg} = 3.2 \times 10^{-12} S_{\rm rad}^6 (1 + S_{\rm rad}/55) \text{ s} \quad (6)$$

and

$$\tau_\gamma \approx \frac{r_{\rm scale}^2}{\lambda_{\rm mfp}^2} \frac{\lambda_{\rm mfp}}{c}, \quad (7)$$

where $E_{\rm reg}$ and $L_{\rm reg}$ are the energy and neutrino luminosity near the surface of the neutron star over the scale height $r_{\rm scale}$ (see eq. [40]), $S_{\rm rad}$ is the radiation entropy of the atmosphere, $\lambda_{\rm mfp}$ is the mean free path of the photons, and c is the speed of light. For entropies in which $\tau_\gamma > \tau_\nu$ ($S < 600$; see Fig. 1), the photons will be carried in with the accreting material and we can assume reliably that the photons are trapped. However, this argument relies implicitly upon a spherically symmetric flow. When convection becomes important, we must once again examine the effects of this convection-enhanced photon diffusion. We will consider these specific cases as they appear in our equilibrium simulations.

For the infall atmospheres, we can use the infall rate to determine the inward motion of the material and compare it to photon diffusion. The trapping radius is then the radius at which speeds are equal and is commonly denoted (e.g., see Chevalier 1989)

$$r_{\rm tr} = \min\left(\frac{\dot{M}\kappa}{4\pi c}, r_{\rm B}\right), \quad (8)$$

where $\dot{M}$ is the mass infall rate, κ is the opacity of the infalling material (we assumed $K = 0.2$ cm^2 g^{-1}), c is the speed of light, and $r_{\rm B}$ is the Bondi accretion radius. From Table 1, we see that the trapping radius for most neutron star encounters with stellar objects is close or equal to the Bondi radius and, as a result, the diffusion of photons is unimportant.

3.3.4. *Magnetic Fields*

We have assumed in our simulations that the magnetic field of the neutron star has no effect upon the hydrodynamics. This assumption is valid for two regimes: for

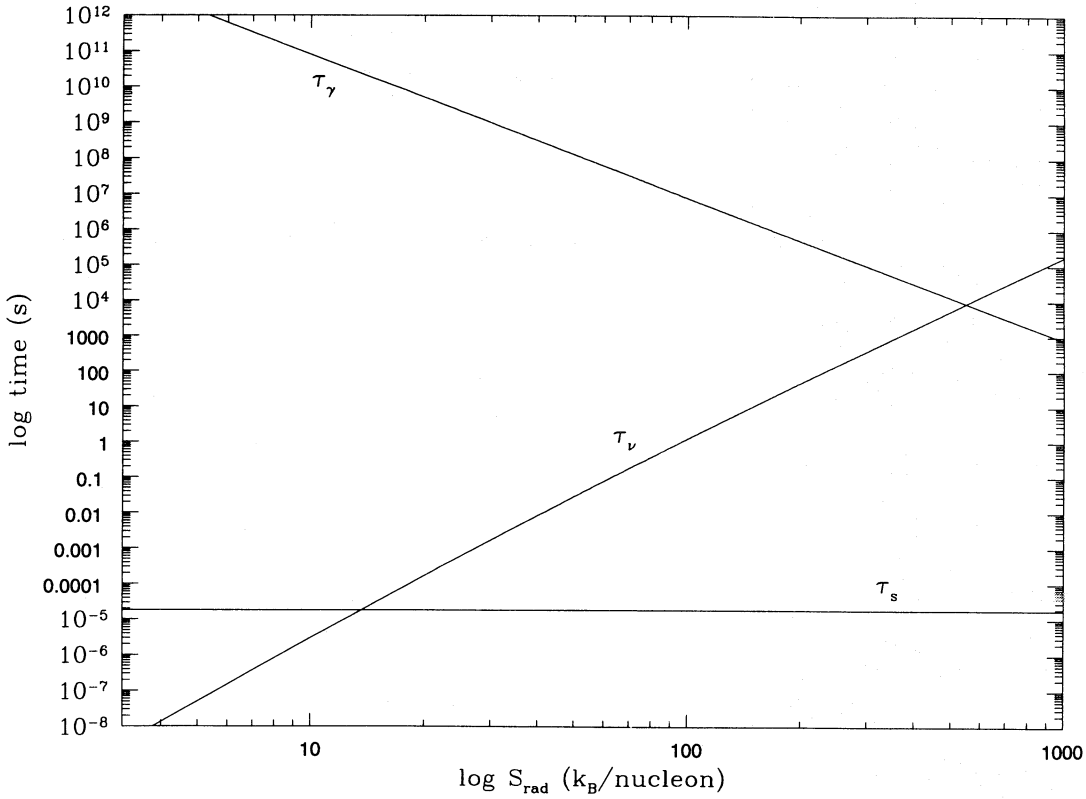

FIG. 1.—Characteristic timescales: photon diffusion τ_γ, neutrino cooling τ_ν, and sound travel time τ_s vs. entropy. Note that at an entropy lower than that defined by the intersection between the sound travel and neutrino cooling timescale, no stable atmosphere can form. Note also that the intersection between photon diffusion and neutrino cooling defines the entropy at which photon trapping is complete.

neutron stars with low magnetic fields and for high infall rates which smother the magnetic field of the neutron star. The importance of magnetic fields can be estimated by finding the radius at which the magnetic energy density equals the kinetic energy density of the infalling matter (Shapiro & Teukolsky 1983, p. 405):

$$\frac{B^2}{8\pi} = \frac{1}{2}\rho v_{\rm ff}^2 \tag{9}$$

$$\Rightarrow \frac{\mu^2}{8\pi r_{\rm A}^6} = \frac{1}{2}\frac{\dot{M}}{4\pi r_{\rm A}^2 v_{\rm ff}} v_{\rm ff}^2 , \tag{10}$$

where B is the magnetic field, μ is the magnetic dipole moment, ρ is the density of the matter, $v_{\rm ff}$ is the free-fall velocity, $r_{\rm A}$ is the Alfvén radius, and $\dot{M}$ is the mass infall rate. To ensure that magnetic fields are unimportant, the Alfvén radius should lie within the neutron star. For a 10^{12} G magnetic field, the accretion rate has to be

$$\dot{M} \gtrsim 0.8\ M_\odot\ {\rm yr}^{-1} . \tag{11}$$

Thus, for high infall rates the infalling material effectively smothers even high magnetic fields, and its trajectory is unaffected by them.

However, the above calculation may be overly conservative because it ignores the pileup of material which occurs at lower infall rates. As the infalling material builds up around the neutron star, the pressure at the base of the atmosphere increases. In a more detailed analysis, Chevalier (1989) calculated the relative importance of radiation and magnetic pressure for this built-up material around a neutron star. He found that for the radiation pressure to exceed the magnetic pressure at the surface of a 10^{13} G neutron star, the infall rate need only exceed $5 \times 10^{-6}\ M_\odot\ {\rm yr}^{-1}$, in support of our assumption that magnetic fields are unimportant at high accretion rates.

4. RESULTS

Following the strategy that we mapped out in the introduction, we present two sets of simulations for which the initial atmosphere structures were defined by either free-fall or pressure equilibrium conditions. Recall that the infall atmospheres model the likely initial conditions encountered by a neutron star entering a medium. The infall simulations provide clues to the structure of the developing atmosphere which, in most cases, will become similar to our second set of models, the equilibrium atmospheres. From the equilibrium atmosphere simulations, we can then determine the ultimate fate of these systems. In both cases, we found that the outcome is primarily dependent upon one parameter: the infall rate for the infall atmospheres and the entropy for equilibrium atmospheres. In this section, we also compare our results to prior analytical derivations obtained by C89 and HC for infall atmospheres and CHB for equilibrium atmospheres.

4.1. *Infall Atmospheres*

The structure of infall atmospheres has been discussed analytically by C89 and in more detail by HC and Brown (1995). The qualitative structure, and indeed most of the quantitative results, predicted by C89 are in good agreement with our numerical simulations. The density and pressure profiles derived by C89, with only a slight modification of the adiabatic index, match our numerical simulations closely. Still, as we shall see further, the seemingly innocuous deviation of the adiabatic index for very high infall rates has nonnegligible consequences on the overall hydrodynamical evolution. Yet of greater importance, convection adds a new dimension to the problem as high-entropy bubbles drive the accretion shock outward. We begin this section with a summary of conditions prevailing in steady state infall atmospheres, much in the same was as the ideas set forth by C89. Then we go on to the analysis of the initial transient which occurs during the onset of accretion and has important consequences for the subsequent evolution. Then we discuss our one-dimensional simulations and compare them to the work of C89. We end this section by discussing the effects of convection on infall atmospheres.

4.1.1. *Steady State Infall Structure*

As a neutron star plows through an ambient medium, material within the Bondi infall radius is captured and falls inward. Initially, pressure forces are insignificant so that the infall structure is similar to that predicted by the free-fall solution. Rapidly, however, "the sink backs up" as the Bondi infall rate [$\dot{M}_{\rm B} = 4\pi r_{\rm B}^2 \rho_{\rm ext}(c_{\rm ext}^2 + v_{\rm NS}^2)^{1/2}$, where the "ext" subscript indicates the external density and sound speed] exceeds the acceptance rate determined by the cooling rates. As matter continues to crash down, it heats up, and pressure increases until it is sufficient to slow down the infall by a shock. The accretion shock moves outward from the neutron star, until the flow structure (especially conditions in the neighborhood of the neutron star) allows neutrino losses to match the energy output due to accretion, or in the case of low infall rates, until the shock emerges from the optically thick domain. In the latter case, which we will not consider further, the accretion is Eddington limited, while in the former case, neutrino cooling allows an essentially unlimited accretion rate.

The accretion shock separates two distinct structural regions in the infall (see Fig. 2). Outside the shock, the infall can be characterized by the free-fall solution (see, for example, C89)

$$v_{\rm ff} = \sqrt{\frac{2GM}{r}} \tag{12}$$

and

$$\rho_{\rm ff} = \frac{\dot{M}_{\rm B}}{4\pi r^2 v_{\rm ff}} , \tag{13}$$

where G is the gravitational constant, M is the neutron star mass, and r is the distance from the center of the neutron star.

At the shock, using mass, momentum, and energy conservation in addition to a perfect gas equation of state and assuming a strong shock, the shock jump conditions are (C89)

$$P_{\rm sh} = \frac{\gamma + 1}{2}\rho_{\rm ff} v_{\rm ff}^2 \tag{14}$$

and

$$\rho_{\rm sh} = \frac{\gamma + 1}{\gamma - 1}\rho_{\rm ff} , \tag{15}$$

where the pressure outside the shock is considered to be negligible (strong shock assumption) and γ is the adiabatic index.

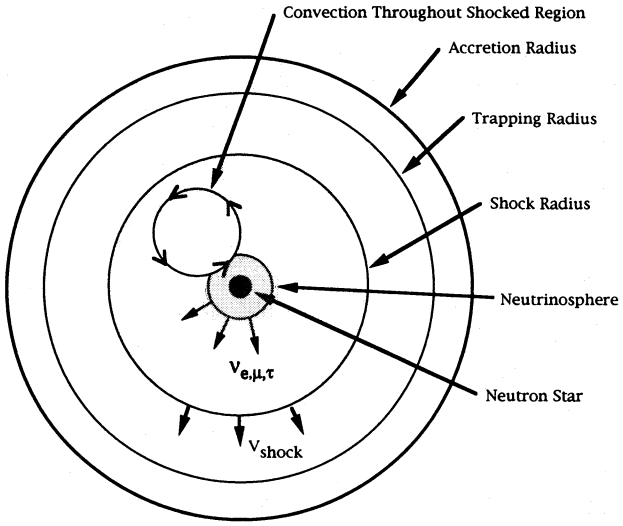

FIG. 2.—Structure of an infall atmosphere. Note that the region within the accretion shock is convectively unstable.

Inside the shock front, in the setting region, we turn again to the conservation equations assuming spherical symmetry and that all initial transients set by the outmoving shock wave are quickly ironed out by convection (C89):

$$\partial\rho/\partial t + \nabla(\rho v) = 0 \quad \text{mass conservation}\,, \tag{16}$$

$$\partial v/\partial t + \nabla(v^2/2 + P/\rho) = F_T \quad \text{momentum conservation}\,, \tag{17}$$

and

$$P \propto \rho^{\gamma} \quad \text{adiabatic perfect gas}\,, \tag{18}$$

where F_T is the net external force (in our case, gravity). Steady state solutions demand that $\partial v/\partial t = \partial\rho/\partial t = 0$, so that the mass conservation equation becomes $4\pi r^2\rho v = \text{const} = \dot{M}_B$. Moreover, right behind the shock radius, we have that $v^2/2 \ll P/\rho$, since the flow becomes subsonic ($v^2 < c_s^2 = \gamma P/\rho \propto \rho^{\gamma-1}$). From the mass conservation equation, $v^2 \propto \rho^{-2}r^{-4}$ so that the ratio $(v^2/2)/(P/\rho) \propto r^{-4}\rho^{-1-\gamma}$. Since ρ is obviously a decreasing function of radius, we have that $V^2/2 \ll P/\rho$ everywhere behind the shock. Thus, one can neglect the v^2 term in the momentum conservation equation (17) throughout the region behind the shock, so that the determination of the density and pressure becomes straightforward (C89):

$$\rho = \rho_{sh}\left(\frac{r}{r_{sh}}\right)^{-1/(\gamma-1)} \tag{19}$$

and

$$P = P_{sh}\left(\frac{r}{r_{sh}}\right)^{-\gamma/(\gamma-1)}\,. \tag{20}$$

As the pressure, and hence temperature, at the base of the atmosphere increases, the neutrino emission increases. Because of the low cross section of interaction with matter ($\sigma_\nu = 10^{-43}$ cm^2 vs. $\sigma_\gamma = \sigma_T = 6 \times 10^{-25}$ cm^2), the neutrinos are not trapped like the photons and commence cooling the base of the atmosphere. An important cooling mechanism is the capture of electrons and positions by free protons and neutrons with emission of electron neutrinos and anti-electron neutrinos, respectively. In the regime in which pairs dominate and the matter is completely dissociated into free nucleons (corresponding to a high temperature and entropy), the emission rate can be approximated by (Herant et al. 1992)

$$\frac{d\epsilon_{nuc}}{dt} = 2 \times 10^{18} T_{MeV}^6 \text{ ergs g}^{-1}\text{ s}^{-1}\,. \tag{21}$$

Also important is the annihilation of electrons and positrons into neutrino antineutrino pairs of all flavors which, if pairs dominate, can be written as (Herant et al. 1992)

$$\frac{d\epsilon_{pp}}{dt} = 1.9 \times 10^{25}\,\frac{T_{MeV}^9}{\rho} \text{ ergs g}^{-1}\text{ s}^{-1}\,. \tag{22}$$

In steady state, the neutrino losses balance the gain in potential energy due to accretion:

$$4\pi r_{NS}^2(\Delta r_{ER})\rho\,\frac{d\epsilon_{tot}}{dt} = \frac{GM_{NS}\dot{M}_B}{r_{NS}}\,, \tag{23}$$

where Δr_{ER} is the thickness of the emission region at the base of the atmosphere where most of the cooling takes place (one temperature scale height, $\sim r_{NS}/8$), $d\epsilon_{tot}/dt$ is the specific neutrino cooling rate from the neutrino emission processes (eqs. [21] and [22]). This last expression closes the set of equations that determines the steady state of the system and allows one to determine r_{sh}. For instance, we can use the approximation that the pressure is dominated by radiation at the base of the atmosphere (i.e., $P_{atm} = aT_{atm}^4$, $\gamma = 4/3$) to determine the temperature at the base of the atmosphere from equations (12)–(20), and thus the cooling rate for free nucleon emission

$$\frac{d\epsilon_{nuc}}{dt} = 8.5 \times 10^{15}\left(\frac{M}{1.4\,M_\odot}\right)^{3/4}\left(\frac{\dot{M}_B}{M_\odot\text{ yr}^{-1}}\right)^{3/2} \times \left(\frac{r_{NS}}{10\text{ km}}\right)^{-6}\left(\frac{r_{sh}}{100\text{ km}}\right)^{9/4} \text{ergs g}^{-1}\text{ s}^{-1}\,, \tag{24}$$

and pair annihilation,

$$\frac{d\epsilon_{pp}}{dt} = 9.2 \times 10^{16}\left(\frac{M}{1.4\,M_\odot}\right)^{13/8}\left(\frac{\dot{M}_B}{M_\odot\text{ yr}^{-1}}\right)^{5/4} \times \left(\frac{r_{NS}}{10\text{ km}}\right)^{-6}\left(\frac{r_{sh}}{100\text{ km}}\right)^{15/8} \text{ergs g}^{-1}\text{ s}^{-1}\,. \tag{25}$$

For most steady state accretion scenarios, the pair annihilation emission process dominates the cooling, so we will ignore nucleon emission in determining r_{sh}. Assuming a 10 km, 1.4 $M_\odot$ neutron star, we obtain a result similar to C89:

$$r_{sh}^{\gamma=4/3} = 6.7 \times 10^8 \dot{M}_B^{-10/27}\text{ cm}\,, \tag{26}$$

where $\dot{M}_B$ is in $M_\odot$ yr^{-1}. Our neutrino emission processes are slightly different from those in C89 which, combined with a different value for the emission region (we used r_{NS}), accounts for the slight differences between the two solutions. We can repeat this derivation for various values of gamma to obtain

$$r_{sh}^{\gamma=1.37} = 3.3 \times 10^9 \dot{M}_B^{-0.46}\text{ cm} \tag{27}$$

and

$$r_{sh}^{\gamma=1.4} = 1.7 \times 10^{10} \dot{M}_B^{-0.56}\text{ cm}\,. \tag{28}$$

4.1.2. *The Onset of Accretion and the Initial Transient*

We now leave the steady state solution and return to the analysis of the initial transient which takes place at the

beginning of the evolution. During the initial phase of the accretion, the shock moves out from the surface of the neutron star toward its steady state position r_{sh}. As a result, the postshock entropy decreases as the accretion shock progresses outward and weakens. Assuming that radiation dominates, but that electrons are nonrelativistic (which is reasonable away from direct proximity of the neutron star), the postshock entropy can be written $S_{sh} = 1.1 \times 10^{-11} P_{sh}^{3/4}/\rho_{sh}$. We can then apply the shock equations (14) and (15) and the free-fall equations (12) and (13) to determine the entropy for a given shock radius and infall rate:

$$S = 5.5 \times 10^3 \frac{[(\gamma + 1)/2]^{3/4}}{(\gamma + 1)/(\gamma - 1)} M_{NS}^{7/8} \dot{M}_B^{-1/4} r_6^{-3/8}, \quad (29)$$

where S is in k_B per nucleon, M_{NS} is the mass of the neutron star in solar masses, $\dot{M}_B$ is the infall rate in $M_\odot$ yr^{-1}, and r_6 is the radius of the shock in units of 10^6 cm. Note that in the strong shock regime (which applies if the shock radius remains much smaller than the Bondi radius), the entropy below the shock is independent of the entropy above the shock. Consequently, in most of our simulations, the initial entropy of the infalling material has little effect on the resulting structure.

Because of the dependence on radius (exponent $-\frac{3}{8}$) of the postshock entropy, the outward motion of the shock imprints a negative entropy gradient in the inner region during the initial transient. This entropy profile is evidently unstable and leads to a break in the spherical symmetry which is not included in the picture developed in C89. The timescale for convection can be approximated using the Brunt-Väisäla frequency N (see Cox, Vauclair, & Zahn 1983):

$$N^2 = \frac{g}{\rho}\left(\frac{\partial \rho}{\partial S}\right)_P \frac{\partial S}{\partial r}. \quad (30)$$

For $\partial S/\partial z < 0$, $N^2 < 0$ and the atmosphere is unstable. The timescale for this convection (τ_{conv}) is $(|1/N^2|)^{1/2}$. Of course, convective instability can also depend on the chemical composition, as an atmosphere may be stabilized by a negative gradient of the molecular weight. However, the entropy gradients are sufficiently high in our simulations that this is not a concern. The region within the accretion shock convects until stability is achieved and ultimately develops into an equilibrium atmosphere.

An additional effect of this initial convection is to drive the shock beyond its steady state value, lowering the entropy at the shock (eq. [29]) with respect to the steady state prediction. This material ultimately makes its way down to the base of the atmosphere, defining the entropy of the equilibrium atmosphere. Since the base of the atmosphere depends on its entropy, this convection-driven overshoot can drastically alter the evolution of the system. Equilibrium atmospheres and the effect of the initial transient on their entropy will be addressed in § 4.2.

However, this description does not apply to extremely high infall rates. Beginning from the free-fall solution of matter crashing down on the neutron star, surface, we have

$$\frac{GM_{NS} r_{NS}}{\rho_{atm}} = aT_{atm}^4, \quad (31)$$

so that the temperature at the bottom of the atmosphere is proportional to the density at the bottom of the atmosphere to the one-fourth power: $T_{atm} \propto \rho_{atm}^{1/4}$. From mass conservation, we also have that $\rho_{atm} \propto \dot{M}$, and as a result $T_{atm} \propto \dot{M}^{1/4}$. Since neutrino cooling has a high power dependence on temperature (see § 4.2), there exists a critical mass infall rate beyond which the accretion shock can hover right above the neutron star and provide a sufficiently high temperature for neutrino cooling to allow accretion to take place immediately. In our simulations, this occurs at infall rates upward of 10^5 $M_\odot$ yr^{-1} (see Table 2). The critical infall rates are slightly higher for the higher initial entropy atmospheres because of their lower initial neutrino luminosities.

Thus, rapid mass infall atmospheres lead to three distinct regimes. For a low rate of infall, material builds up around the neutron star and sends an accretion shock outward from the core. The unstable negative entropy gradient inprinted by the motion of the shock leads to instabilities. The low-entropy matter at the shock is convected downward onto the neutron star, and eventually an equilibrium atmosphere forms, with the range of outcomes discussed in § 4.2. Intermediate rates of infall initially lead to similar situations. However, the intense neutrino emission leads to cooling times that are shorter than the convective time, thus preventing the formation of an equilibrium atmosphere. For a high rate of infall, the material is shocked at close proximity of the neutron star surface and cools efficiently through neutrino emission without further ado.

4.1.3. *One-dimensional Simulations*

We have modeled a series of infalls for a range of infall rates and initial entropies. The results from the one-dimensional simulations are shown in Table 2. Note that the initial entropy has little impact, except in mass accretion rates near the transition between high and intermediate infall regimes.

Although the structure of the infall atmosphere is reasonably well described by the analytical derivation of C89, we found that the effective adiabatic index γ from our more detailed equation of state is slightly higher than the radiation dominated 4/3 assumed by C89 (see Fig. 3). For infall rates below 1 $M_\odot$ yr^{-1}, this deviation is too small to have a

TABLE 2

INFALL ATMOSPHERES (ONE-DIMENSIONAL RESULTS)

Infall Rate ($M_\odot$ yr^{-1})	L_ν^{tot} (ergs s^{-1})	τ_{conv} (s)	γ	S_{center}
$S_{infall} = 30$, $M_{crit} = \sim 10^6$				
10^0	$< 10^{39}$	~ 0.02	1.35	630
10^1	$\sim 3 \times 10^{41}$	~ 0.06	1.37	380
10^2	$\sim 7 \times 10^{43}$	~ 0.05	1.4	220
10^3	$\sim 6 \times 10^{46}$	~ 0.03	1.4	120
10^4	$\sim 2.5 \times 10^{48}$	~ 0.03	1.4	85
10^5	$\sim 1 \times 10^{50}$	~ 0.03	1.43	~ 50
$S_{infall} = 10$, $M_{crit} = \sim 5 \times 10^5$				
10^0	$< 10^{39}$	~ 0.02	1.35	650
10^2	$\sim 9 \times 10^{43}$	~ 0.03	1.4	200
10^5	$\sim 3 \times 10^{50}$	~ 0.03	1.4	~ 40
10^6	$\sim 7 \times 10^{51}$	~ 0.02	1.43	~ 25
$S_{infall} = 50$, $M_{crit} = \sim 2 \times 10^6$				
10^1	$\sim 2 \times 10^{41}$	~ 0.02	1.37	650
10^3	$\sim 2 \times 10^{46}$	~ 0.03	1.4	130

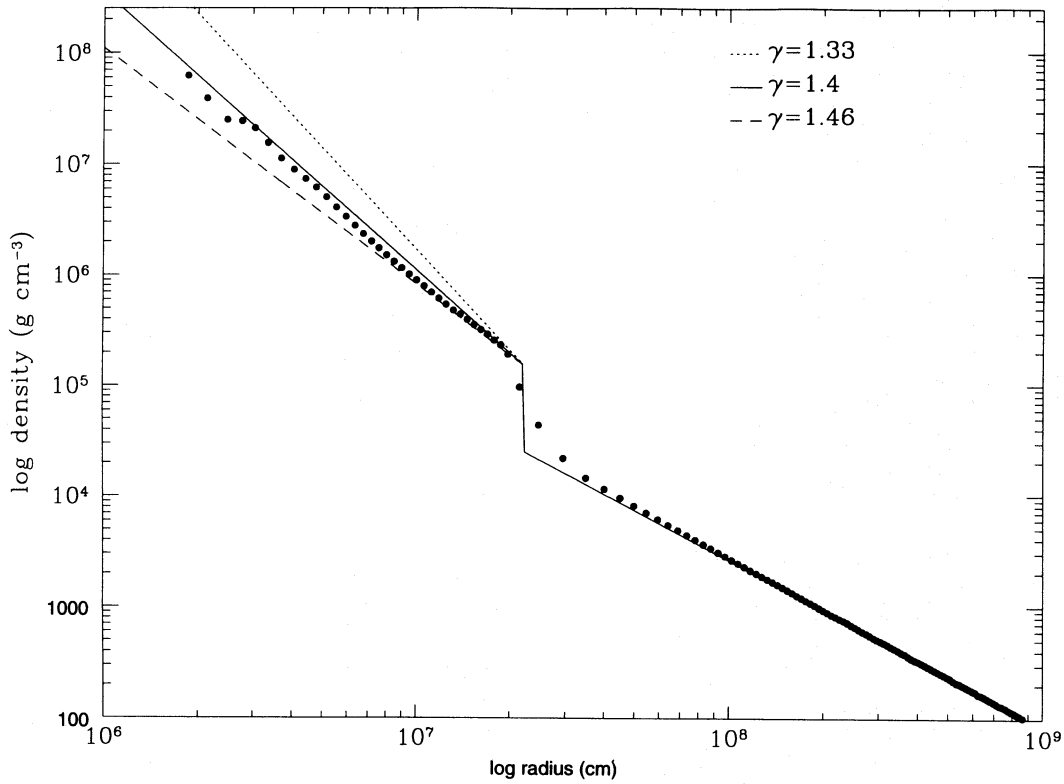

FIG. 3.—Density vs. radius for a $10^3\ M_\odot\ \mathrm{yr}^{-1}$ infall model. The points are from numerical simulations. The lines are analytical results for different adiabatic indices.

significant impact on the flow structure, but for higher infall rates, it has a crucial influence on the steady state position of the shock. Figure 4 shows r_{sh} versus accretion rates for a range of adiabatic indices (1.33, 1.37, 1.40) using equations (26)–(28). Note that by merely changing from γ from 4/3 to 4.2/3 for the 100 $M_\odot\ \mathrm{yr}^{-1}$ simulation changes r_{sh} by an order of magnitude. This is important because, as we have seen in the previous section, the position at which the shock stalls determines the entropy of the atmosphere which develops in the inner region in the vicinity of the neutron star. As we shall discuss in § 4.1.4, this entropy determines the ultimate fate of the atmosphere.

Figure 5 shows the entropy profile established by the transient motion of the shock from the surface of the neutron star toward its steady state radius. As predicted by equation (29), the entropy gradient is negative and will thus be subject to convective instabilities. Table 2 lists Brunt-Väisäla timescales along with neutrino luminosities, effective γ values, and central entropies for all the one-dimensional simulations. It is clear, however, that multidimensional simulations are needed to calculate the subsequent evolution.

4.1.4. *Two-dimensional Simulations*

Since the high infall regime is not conducive to instabilities, we have limited our two-dimensional simulations to intermediate and low rates of infall. These atmospheres become active quickly (recall the short Brunt-Väisäla timescales), sending bubbles outward through the inner region. These bubbles contribute to the outward push of the shock, while plumes of low-entropy material stream down towards the neutron star (see Fig. 6). To better appreciate the properties of infalling atmospheres, the distinction between intermediate and low infall atmospheres needs to be elucidated. In addition, for the low infall regimes, we would like to determine the entropy of the resulting equilibrium atmosphere. As stated in the introduction, owing to the relatively long convecting timescales ($>10^4$ s), it is impossible to simulate a complete convective turnover as the Courant time step restriction near the neutron star is of order of tens of microseconds. Nevertheless, the simulations provide sufficient indications about the long-term behavior of the system to allow us to predict the ultimate outcome of the evolution.

In our simulations, we have noticed that the typical velocity of an infalling plume of material traveling between the shock and the neutron star is ~ 0.1 the free-fall velocity, Knowing this, we can estimate the convective turnover timescale (see Table 3):

$$\tau_{\mathrm{conv}} = 10 t_{\mathrm{dyn}} = 10 \frac{\pi r}{c_s} = 10 \frac{\pi r^{1.5}}{\sqrt{G M_{\mathrm{ns}}}}, \qquad (32)$$

where t_{dyn} is the dynamical timescale, r is the radius of the material to be convected inward, and τ_{conv} is the time to advect material from the shock to the neutron start surface. The time τ_{conv} must be compared with the time τ_{BH} required for the neutron star to accrete enough material to collapse into a black hole (see Table 3):

$$\tau_{\mathrm{BH}} = \frac{1}{L_\nu} \frac{G M_{\mathrm{NS}} m}{r_{\mathrm{NS}}}, \qquad (33)$$

where L_ν is the total neutrino emission per unit time, m is the additional mass required to induce collapse (we use 0.2 $M_\odot$), and r_{NS} is the neutron star radius. When $\tau_{\mathrm{conv}} > \tau_{\mathrm{BH}}$, which corresponds to the case of intermediate rate of infall, we expect the neutron star to collapse into a black hole before an equilibrium atmosphere can be formed. How-

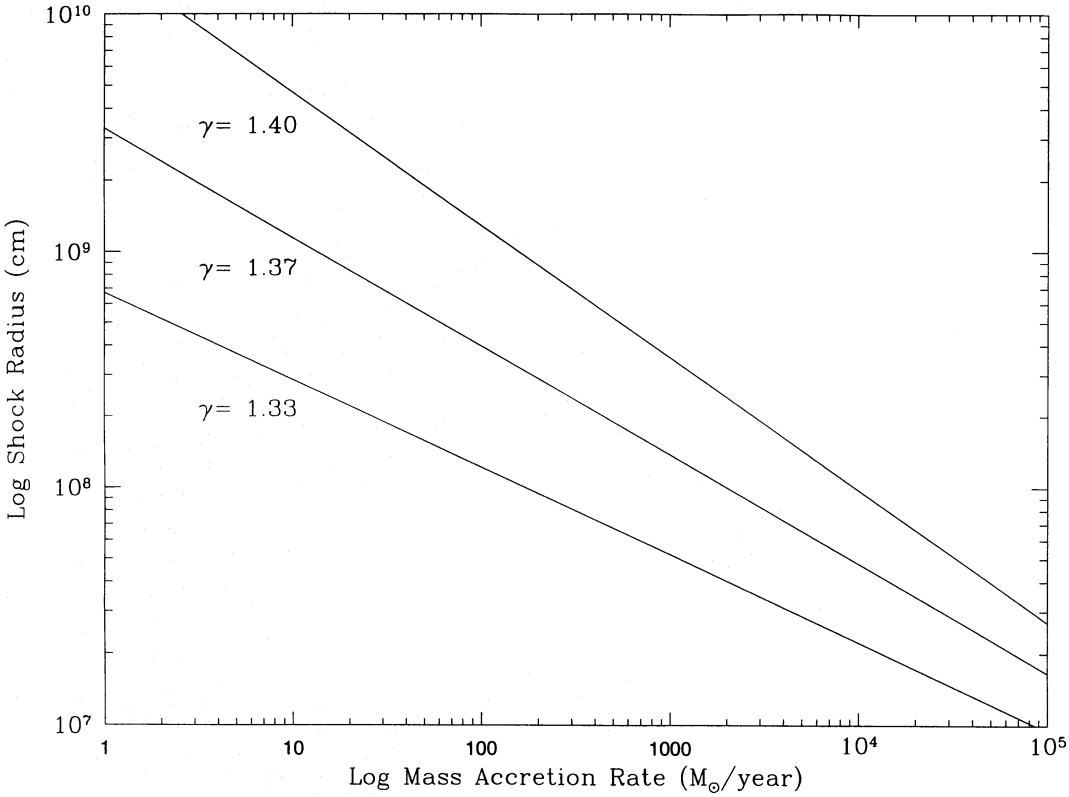

FIG. 4.—Steady state shock radius vs. accretion rate for a change of adiabatic indices in a one-dimensional infall model

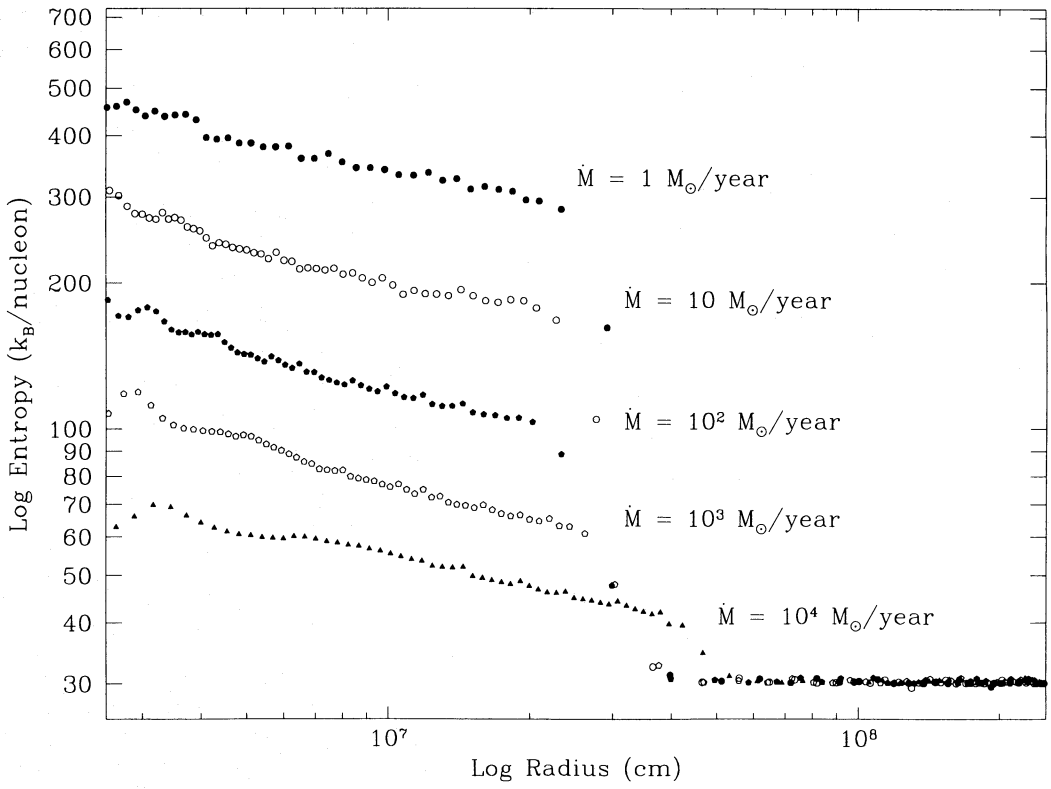

FIG. 5.—Entropy vs. radius after 50 ms for a range of infall atmospheres

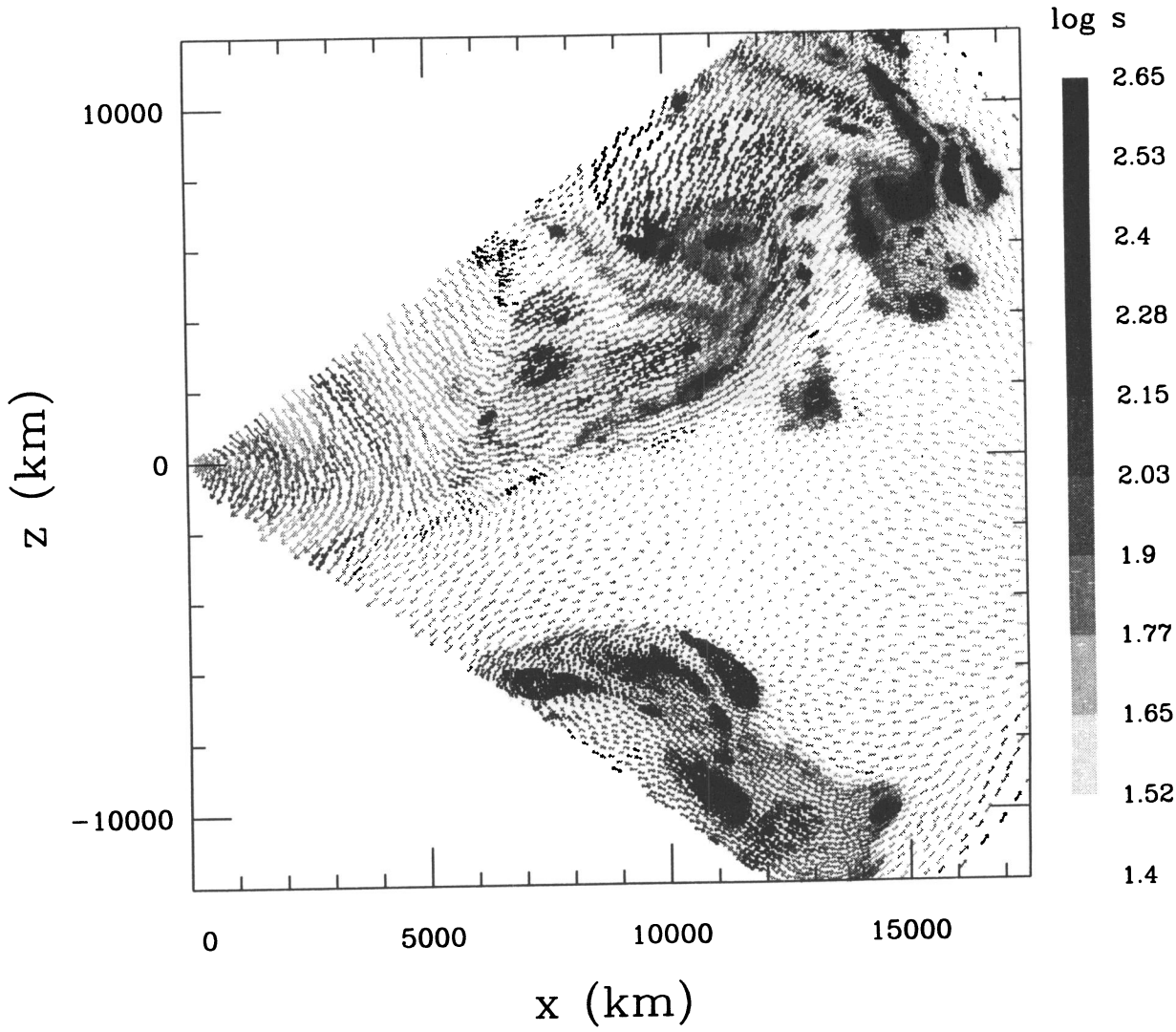

FIG. 6.—Entropy-driven convective plume for $10^3\ M_\odot\ \mathrm{yr}^{-1}$ infall atmosphere 10 s after creation of the accretion shock. The negative entropy gradient is induced by the initial outward motion of the shock. Average plume velocity is 3000 km s^{-1}, and mean inflow velocity is 1000 km s^{-1}.

ever, when $\tau_{\mathrm{conv}} < \tau_{\mathrm{BH}}$, which corresponds to low rates of infall, there is sufficient time for convection to form an equilibrium atmosphere. In these cases, we can use equation (29) to determine the resultant entropy for the equilibrium atmosphere.

These results can be approximately summarized as follows. Very high rates of infall ($\dot{M} \gtrsim 10^6\ M_\odot\ \mathrm{yr}^{-1}$; note that these numbers are estimates as these rates depend on additional factors such as the Bondi radius and initial atmosphere entropy) clamp the shock close to the neutron star and lead to rapid accretion and black hole formation. An intermediate rate of infall ($10^3\ M_\odot\ \mathrm{yr}^{-1} \lesssim \dot{M} \lesssim 10^6\ M_\odot\ \mathrm{yr}^{-1}$) does not have the time to form a proper atmosphere, as it leads rapidly to collapse into a black hole. Low rates of infall ($\dot{M} \lesssim 10^3\ M_\odot\ \mathrm{yr}^{-1}$) allow sufficient time for an equilibrium atmosphere to develop. The structure and fate of these equilibrium atmospheres are discussed in the next section.

4.2. *Equilibrium Atmospheres*

In the previous section, we have studied the initial development of an accretion structure around a neutron star encountering an external medium. We turn now to the ultimate fate of these systems after convective stability has been achieved. Given the condition of initial pressure equilibrium, the most massive atmosphere that can form stably

TABLE 3

INFALL ATMOSPHERES (TWO-DIMENSIONAL RESULTS)[a]

Infall Rate ($M_\odot\ \mathrm{y}^{-1}$)	L_ν^{tot} (ergs s^{-1})	KE_{exp} (ergs)	τ_{BH} (s)	τ_{conv} (s)	S (k_B nucleon^{-1})	M_{exp} ($M_\odot$)
10^1	$\sim 4 \times 10^{41}$	$\sim 3 \times 10^{43}$	$\sim 10^{11}$	10^4–10^6	50–100	10^{-7}
10^3	$\sim 8 \times 10^{45}$	$\sim 2 \times 10^{45}$	$\sim 10^7$	$\sim 10^6$	$\sim S_{\mathrm{infall}}$	0.1
10^5	$\sim 7 \times 10^{49}$	$\sim 2 \times 10^{47}$	$\sim 10^3$	$\sim 10^5$	$\sim S_{\mathrm{infall}}$	100

[a] $S_{\mathrm{infall}} = 30$.

above a neutron star is isentropic, where the entropy is determined by whichever density and temperature is chosen at the surface of the neutron star. More massive atmospheres can be constructed with a negative entropy gradient, but they are unstable to convection. Because even a small negative entropy gradient rapidly drives convection (see eq. [30] for convective timescale), stellar models always adjust themselves to constant entropy or positive entropy gradient structures. We expect the same situation for atmospheres around neutron stars. Consequently, we believe that the most simple and appropriate way to parameterize the set of the possible atmospheres is to use isentropic initial conditions.

The analytical work of CHB has examined the characteristics of constant-entropy equilibrium atmospheres with the additional assumption that the pressure and internal energy are dominated by radiation and electron pairs contributions (that is, $P = 11/12aT^4$). This remains valid at the base of the atmosphere for entropies less than 400 k_B nucleon^{-1} (see eq. [38]) and larger than 30 k_B nucleon^{-1}. The radiation component of the entropy (in units of Boltzmann factor per nucleon) can then be expressed (CHB)

$$S_{rad} = \tfrac{4}{3} \times \tfrac{11}{4} aT^3/(\rho k_B N_A) = 1.4 \times 10^{-11} P^{3/4}/\rho = 5.2 \times 10^8 T_{MeV}^3/\rho \, . \quad (34)$$

This expression is valid when the entropy and temperature are high. For high entropies, $S_{rad} \approx S_{tot}$, so that the analytical derivations can be compared directly to our models with increasing accuracy the higher the entropy.

Assuming constant entropy and a radiation pressure–dominated system, one can use the hydrostatic equation of pressure equilibrium to derive the structure of the atmosphere (CHB):

$$P = [\tfrac{1}{4} M_{NS} G (S_{rad}/S_0)^{-1} (1/r - 1/r_1) + P_1^{1/4}]^4 \text{ dyn cm}^{-2} \, , \quad (35)$$

where $S_0 = 1.4 \times 10^{-11}$ k_B nucleon^{-1} with r_1 and P_1 referring to the radius and pressure at the outer boundary. Implicit in this derivation is that the mass of the atmosphere is negligible when compared to the neutron star mass. As we shall see, for high-entropy atmospheres, this is a good assumption.

In most cases, the radius of the outer boundary is sufficiently large that the terms involving r_1 and P_1 can be neglected. In the equilibrium simulations, we have included varying degrees of boundary pressure (motivated in part by the computed pressure of the infalling material from our infall simulations; § 4.1). Thus, we have incorporated the full equations in our comparison with the analytic solutions. Nonetheless, the basic structure of the atmospheres changes very little (less than a factor of 2 for even the most extreme external pressures) by ignoring the boundary conditions, so we will present the structure equations in their simple, $P_1 = 0, r_1 \gg r_{NS}$ form (CHB):

$$P_{atm} = 1.83 \times 10^{35} S_{rad}^{-4} r_6^{-4} \text{ dyn cm}^{-2} \, , \quad (36)$$

and using equation (34), we find

$$\rho_{atm} = 3.9 \times 10^{15} S_{rad}^{-4} r_6^{-3} \text{ g cm}^{-3} \, , \quad (37)$$

$$T_{atm} = 195 S_{rad}^{-1} r_6^{-1} \text{ MeV} \, , \quad (38)$$

$$M_{atm} = 24.5 \, S_{rad} \ln (r_{max}/r_{NS}) \, M_\odot \, , \quad (39)$$

where r_6 is the radius in units of 10^6 cm, and S_{rad} is the radiation entropy in units of 10^6 cm, and S_{rad} is the radiation entropy in units of k_B nucleon^{-1}. These expressions assume a 1.4 $M_\odot$ neutron star, as in our simulations. The most significant consequence from setting $P_1 = 0$ and $r_1 \gg r_{NS}$ is in the total mass of the atmosphere, M_{atm}. Figure 7 plots M_{atm} as a function of entropy for a outer radius of the atmosphere of 10^9 cm and 10^{13} cm using equation (39) in the case of no external pressure (*dashed lines*) and additional external pressure (*solid lines*). When present, the external pressure was determined using our infall models (see § 4.1) to find the maximum realistic infall pressure ($P_{infall} = \frac{1}{2}\rho_{ff} v_{ff}^2$) at a given radius and entropy. These lines represent the maximum achievable mass for a *stable* atmosphere of the prescribed radius and entropy. Note that despite the fact that constant entropy structures are the most massive stable atmospheres, their masses tend to be small. More massive atmosphere would require a negative entropy gradient, which would then be convectively unstable.

Using equations (21) and (22) combined with the structure equations for temperature and density, it is apparent that the neutrino energy emission per gram falls off roughly as r^{-6}, implying that most of the neutrino emission (and hence cooling of material) occurs close to the neutron star. We estimated the cooling rate by assuming a nearly constant neutrino cooling over a scale height of the emission region (subscript "ER") $r_{ER} = r_{NS}/8$ above the neutron star and calculated the neutrino luminosity per gram in this region. The mass accretion is then

$$\dot{M} = M_{ER} L_{ER}/E_{ER} \, , \quad (40)$$

where M_{ER} is the mass within a scale height of the neutron star, L_{ER} is the neutrino emission from that region using equations (21) and (22), and E_{ER} was chosen (somewhat arbitrarily) to be half the potential energy $GM_{NS} M_{ER}/(r_{NS} + r_{ER})$ gained by the material falling from infinity. Combining these equations and using the $P_1 = 0$ atmosphere structure, we obtain

$$\dot{M} = 9.0 \times 10^{11} S_{rad}^{-10} (1 + S_{rad}/55) \, M_\odot \text{ s}^{-1} \, . \quad (41)$$

Neutrinos emitted at the base of the atmosphere can be recaptured and heat matter higher up. This is especially important for low- and intermediate-entropy atmospheres ($S < 50$). Neutrino absorption by free nucleons gives rise to the following heating term (Herant et al. 1992):

$$\frac{d\dot{\epsilon}}{dt} = 4.8 \times 10^{32} \frac{L_\nu}{4\pi r^2} T_\nu^2 \text{ ergs g}^{-1} \text{ s}^{-1} \, , \quad (42)$$

where L_ν is the electron neutrino luminosity which is caused by neutrino emission at the base of the atmosphere, and T_ν is the neutrino temperature which tends to be similar to the matter temperature near the surface of the neutron star. We have seen earlier that cooling is proportional to r^{-6}, while it appears that heating is proportional to r^{-2}. Therefore, one expects that there exists a radius separating an inner region in which cooling dominates from an outer region where there is a net gain in energy from neutrino processes. This is known in supernova circles as the gain radius.

The preceding equations give an analytical picture of the dominant physical processes involved for atmospheres in which photons are trapped. Note that nuclear burning effects were ignored. In our simulations, we have noticed that the initial chemical composition of the atmospheres

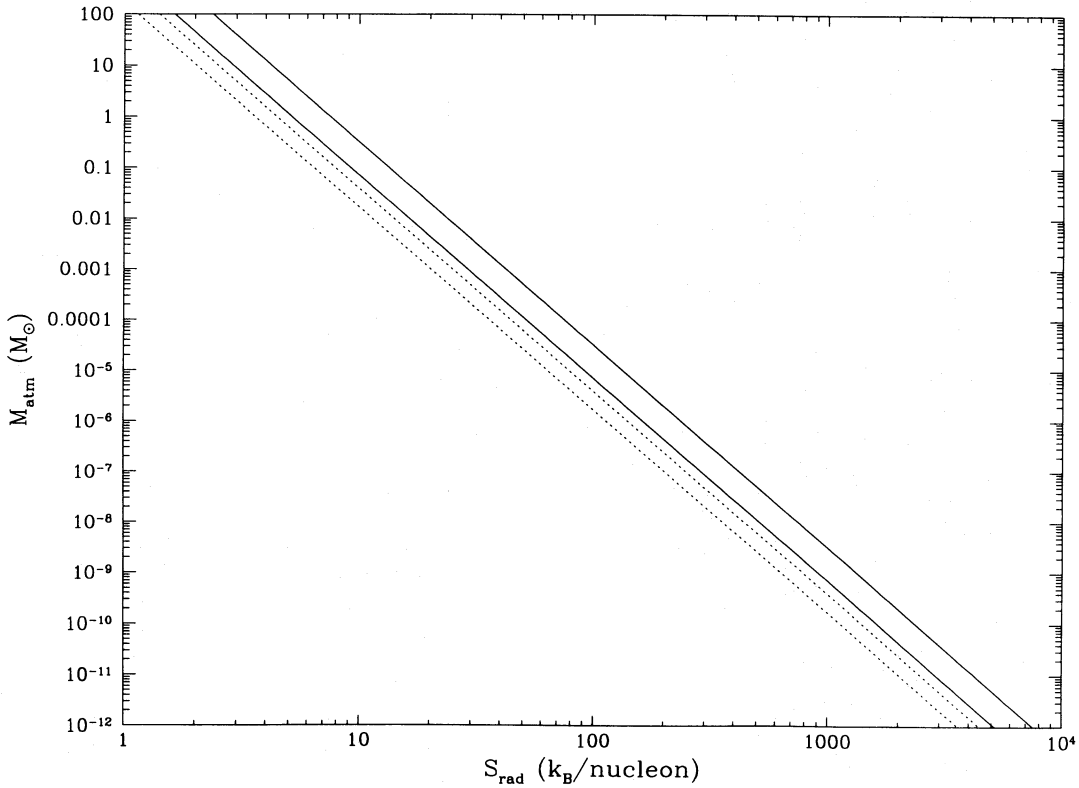

FIG. 7.—Atmospheric mass vs. entropy for two sizes of atmosphere: $R = 10^9$ cm and 10^{13} cm. The dashed lines denote atmospheres with no external pressure, whereas the solid lines include a pressure term derived from typical values for Bondi-Hoyle accretion.

has little effect upon the end result. As was seen analytically, we find that the primary parameter characterizing the atmospheres is entropy. For a low-entropy atmosphere, an immediate explosion is generated by the intense emission of neutrino and the resulting energy deposition just beyond the gain radius. Intermediate ranges for entropy still exhibit noticeable effects from neutrino heating which induce convection. For these entropies, two-dimensional simulations of the atmosphere are required to investigate fully the hydrodynamical evolution. For high-entropy atmospheres, neutrino heating turns out to be unimportant, and hence there is no convection. However, neutrino cooling continues to determine the accretion rates up to extremely high entropies. These results are summarized in Table 4 and presented in more details in the the following sections.

4.2.1. *Low-Entropy Atmospheres*

Figure 1 shows the sound travel time (τ_s) through the neutrino emission region together with neutrino cooling and photon diffusion timescales. For $S_{rad} \lesssim 14\ k_B$ nucleon^{-1}, which corresponds to $S_{tot} \lesssim 22\ k_B$ nucleon^{-1} for our simulations, we find that the neutrino cooling time is faster than the sound travel time. Because of this, it is physically impossible to form such an atmosphere in hydrostatic equilibrium. Thus, it is unlikely that equilibrium atmospheres with low entropies can exist. Just to see what would happen, we have constructed such atmospheres in pressure equilibrium maintained artificially by ignoring neutrino effects. These atmospheres lead to neutrino-driven explosions as soon as neutrino processes are turned on. Despite the fact that they are unphysical, low-entropy atmospheres illustrate the importance of neutrino energy deposition beyond the gain radius. This process also plays a critical role in the more physical scenarios of supernova explosion, or in intermediate-entropy atmospheres which are discussed below.

TABLE 4

CONSTANT ENTROPY ATMOSPHERES

S_{tot}	Results
10.....	Intermediate explosion
20.....	Intermediate explosion
30.....	$\tau_{conv} \approx 5$ ms; $t_{infall} = 0.05$ s; $KE_{exp} = 2 \times 10^{46}$ ergs
50.....	$\tau_{conv} \approx 0.1$ ms; $t_{infall} = 2$ s; $KE_{exp} = 2 \times 10^{45}$ ergs; $\dot{M} \approx 3 \times 10^3\ M_\odot$ yr^{-1}; $L_\nu^{tot} \approx 3 \times 10^{49}$ ergs s^{-1}
60.....	$\dot{M} = 3.8 \times 10^3(\pm 300)\ M_\odot$ yr^{-1}; $L_\nu^{tot} \approx 4 \times 10^{49}$ ergs s^{-1}
70.....	$\dot{M} = 5.2 \times 10^2(\pm 50)\ M_\odot$ yr^{-1}; $L_\nu^{tot} \approx 5 \times 10^{48}$ ergs s^{-1}
80.....	$\dot{M} = 1.8 \times 10^2(\pm 20)\ M_\odot$ yr^{-1}; $L_\nu^{tot} \approx 2 \times 10^{48}$ ergs s^{-1}
90.....	$\dot{M} = 33(\pm 6)\ M_\odot$ yr^{-1}; $L_\nu^{tot} \approx 5 \times 10^{47}$ ergs s^{-1}
100.....	$\dot{M} = 13(\pm 3)\ M_\odot$ yr^{-1}; $L_\nu^{tot} \approx 2 \times 10^{47}$ ergs s^{-1}

4.2.2. *Intermediate-Entropy Atmospheres*

For atmospheres within a range of intermediate entropies ($30 \lesssim S_{tot} \lesssim 50$), the sound crossing time is much less than the neutrino cooling time ($\tau_s \lesssim 0.01\tau_\nu$), allowing the formation of atmospheres in pressure equilibrium. However, neutrino deposition is still sufficiently strong to heat the atmosphere just beyond the gain radius and thus raise the otherwise constant entropy of this region above the value of the rest of the atmosphere. The resulting negative entropy gradient is unstable, and convection takes place. In supernova simulations (HBHFC), this convection increases the efficiency of neutrino heating, leading eventually to an explosion. In the context of our simulations, in order for the convection to be important, it must be able to overcome the general advection inward resulting from the sharp decrease in pressure support as material near the neutron star surface

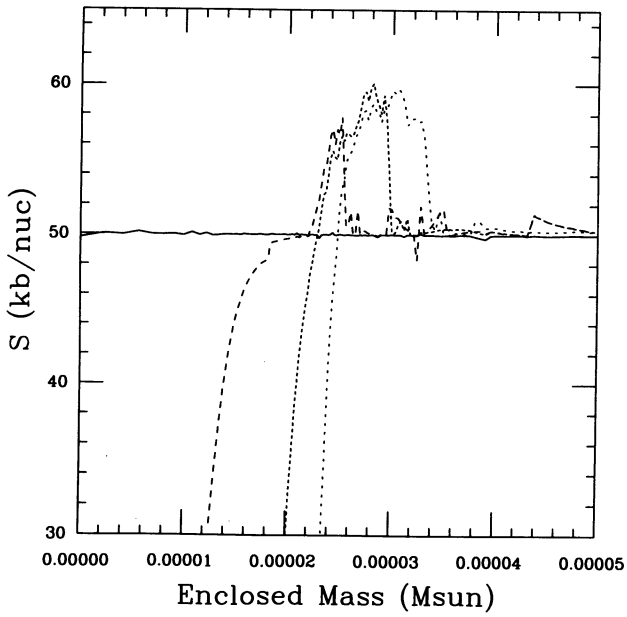

FIG. 8.—Entropy profiles at 70 ms intervals for an $S_{tot} = 50$ equilibrium atmosphere. Note that with increasing time, the innermost material cools (lowering its entropy), while an increasing amount of material is heated (raising its entropy).

is quickly cooled by neutrino emission. Or in simpler terms, the bubbles have to rise faster than they are dragged inward by the general accretion flow. We can estimate the relative importance of these effects in the atmosphere by comparing the Brunt-Väisäla and infall timescales (see Table 4). Evidently, multidimensional simulations are required to model these phenomena correctly.

Figure 8 shows the effects neutrino heating for an $S_{tot} = 50$ atmospheres on the entropy profile in a one-dimensional computation. While neutrino cooling rapidly decreases the entropy at the base of the atmosphere near the neutron star, neutrino absorption further up leads to the formation of an entropy peak and an associated negative entropy gradient which will drive convective instabilities. When the same atmosphere is simulated in two dimensions, large-scale convection arises from the neutrino induced negative entropy gradient, as can be seen in Figure 9. Within this entropy range, the two-dimensional calculations resulted in the expulsion of the atmosphere in what might be considered a "mini-supernova" (see Fig. 10). Table 4 gives explosion energies for atmospheres of different entropies. The energies are much lower than supernova energies, primarily because of the low mass of the atmospheres [$M_{atm}(1000\ km) \sim 10^{-5}$ to $10^{-3}\ M_{\odot}$].

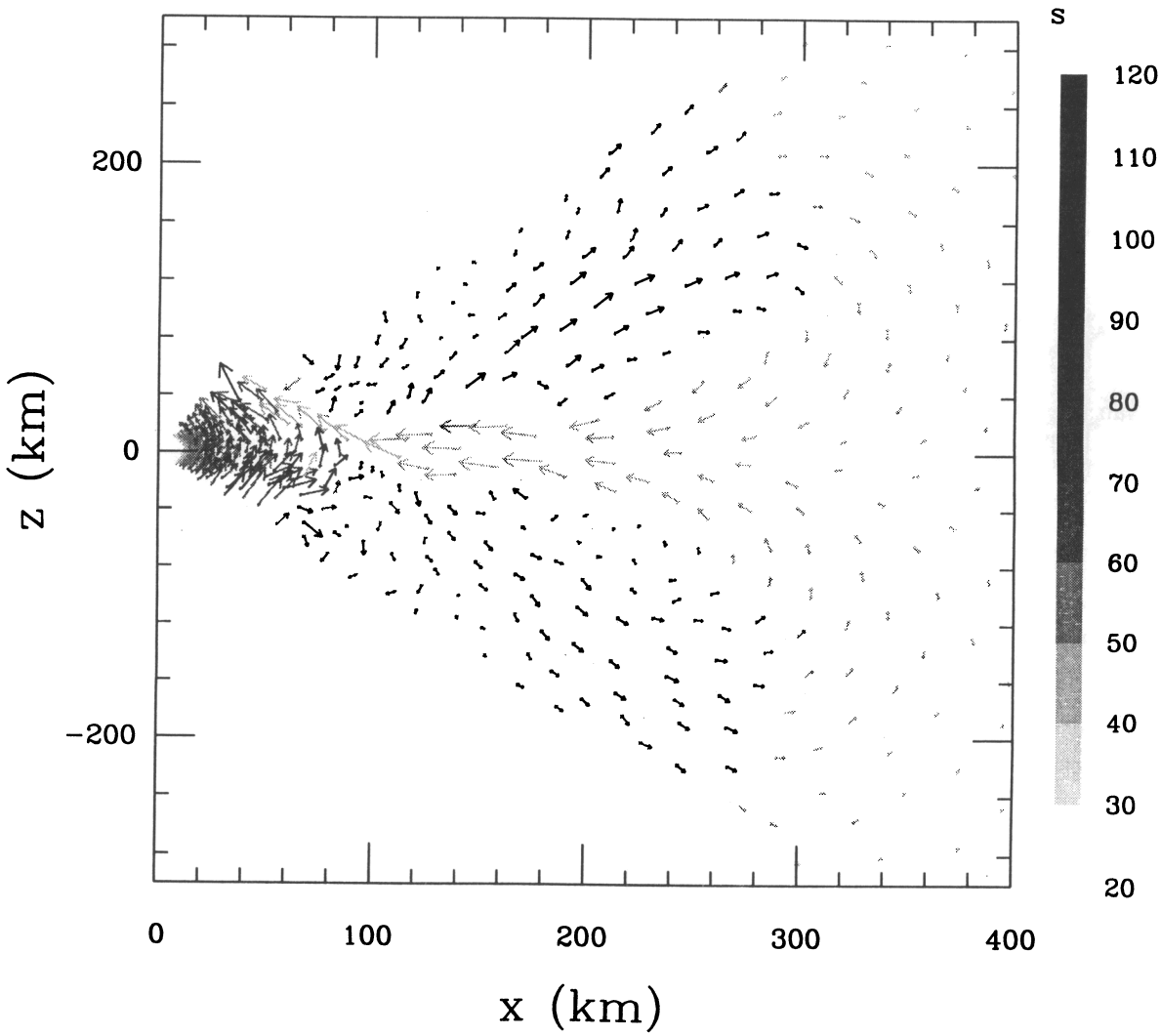

FIG. 9.—Entropy-driven convection for an $S_{tot} = 50$ equilibrium atmosphere 200 ms after turning on neutrino processes. The negative entropy gradient is induced by neutrino heating and drives convection. The mean outflow velocity is 4000 km s^{-1}, and the mean inflow is 9000 km s^{-1}.

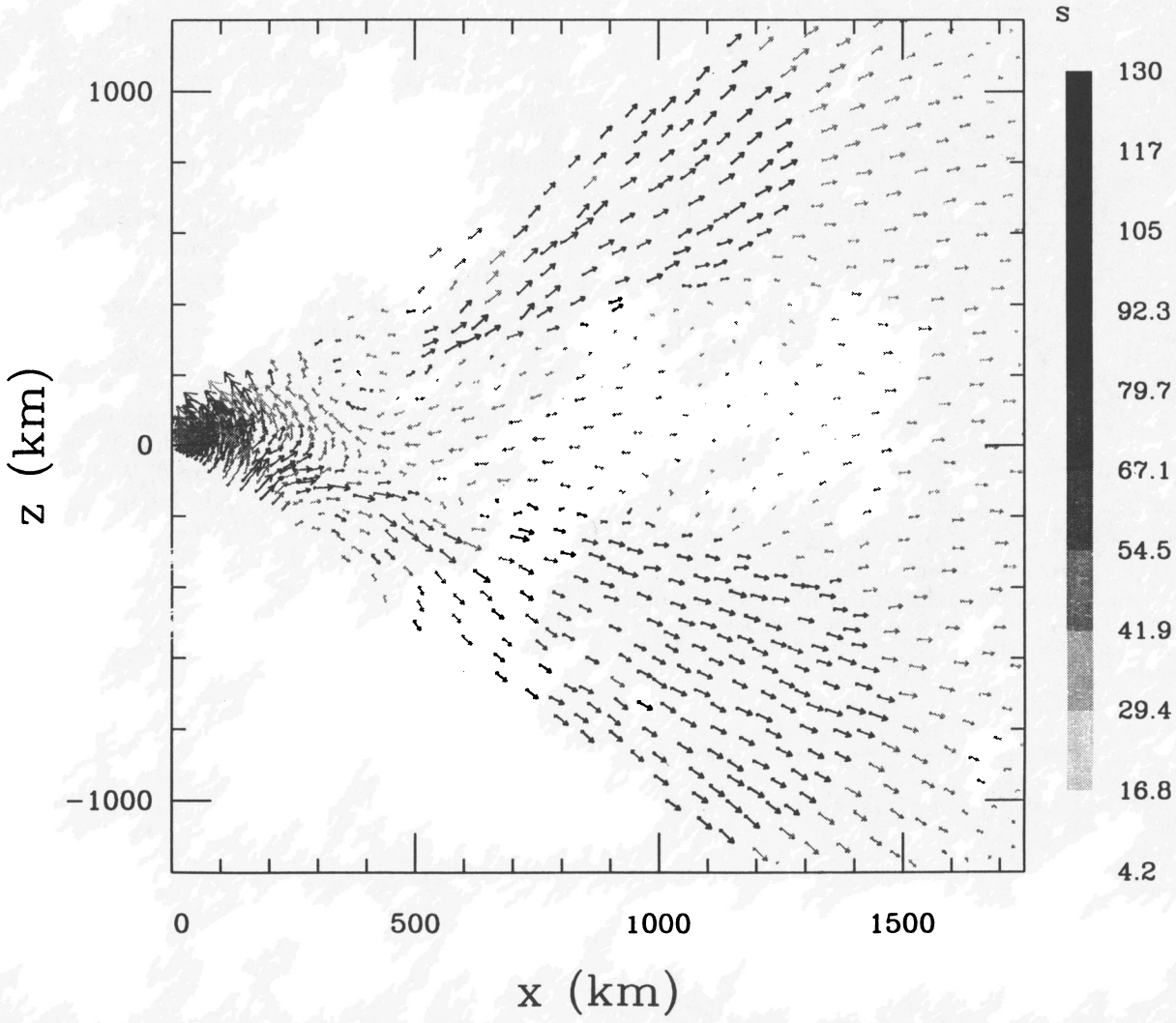

FIG. 10.—The same simulation from Fig. 4 after 500 ms. The atmosphere is now exploding with a kinetic energy of 2×10^{-6} foe (10^{51} ergs). The mean outflow velocity is 5000 km s^{-1}, and the mean inflow is 3000 km s^{-1}.

Rather than trap the released gravitational energy near the surface of the neutron star to be ultimately emitted in neutrinos, convective bubbles transport the energy up through the atmosphere as they rise. Such extensive convection raises the question of whether our one-dimensional analysis which showed photon diffusion to be negligible is still valid. However, given the short timescales required for the explosion to develop in our simulations, photon diffusion remains unimportant. For example, in the worst case scenario of our $S_{tot} = 50$ atmosphere after 0.5 s (see Fig. 11), we find from equations (37) and (7) that photons at 2000 km diffused less than 1.5 km during the course of the simulation, a fraction of the particle size at that radius.

4.2.3. *High-Entropy Atmospheres*

In the case of high-entropy atmospheres ($S_{tot} \gtrsim 60$), neutrino deposition has little effect upon the infalling atmosphere. Neutrino emission, however, remains an efficient source of cooling for all our simulations which extend up to $S_{tot} = 125$. In fact, neutrino losses dominate photon losses up to $S_{tot} = 600$ (Fig. 1).

Figure 12 plots the entropy profile at discrete time intervals (80 ms) for a typical one-dimensional run ($S_{tot} = 80$). The cooled, low-entropy matter consists primarily of neutrons ($Y_e \sim 0.1$) and has essentially become part of the

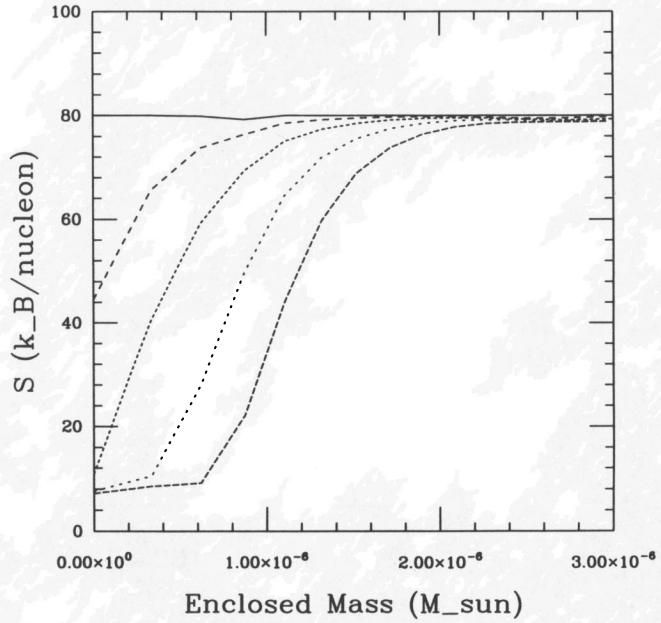

FIG. 11.—Entropy vs. mass at 80 ms intervals for an $S_{tot} = 80$ equilibrium atmosphere. Note that the inner material radiates its energy through neutrino losses, lowering its entropy.

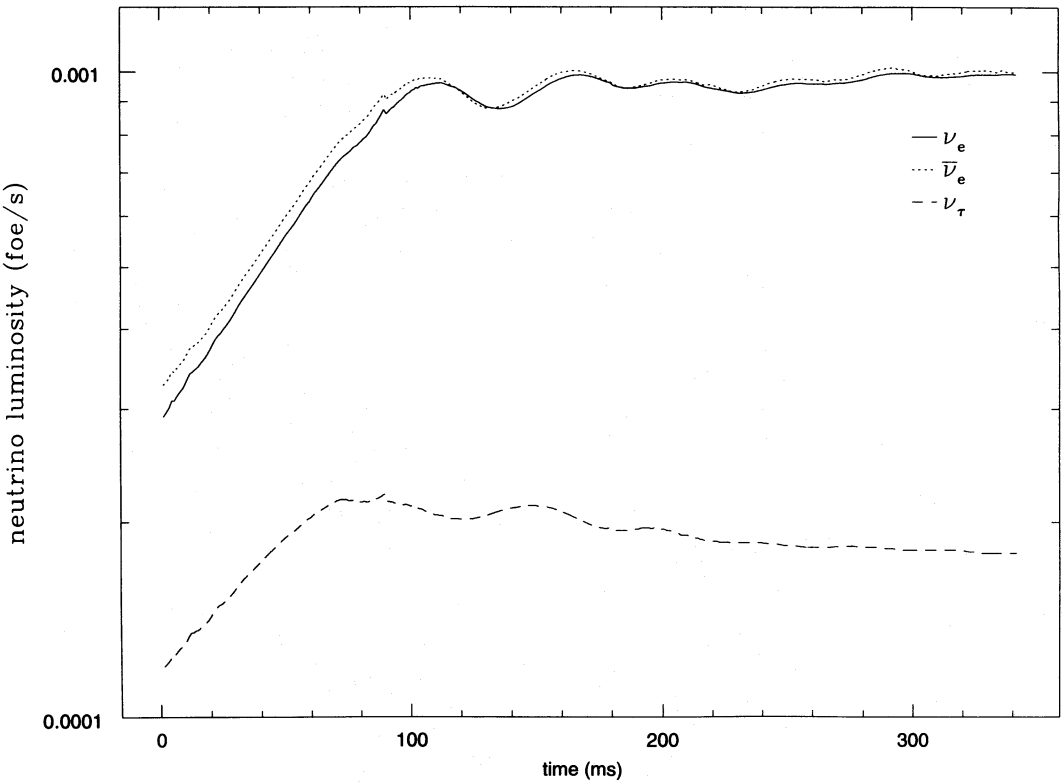

FIG. 12*a*

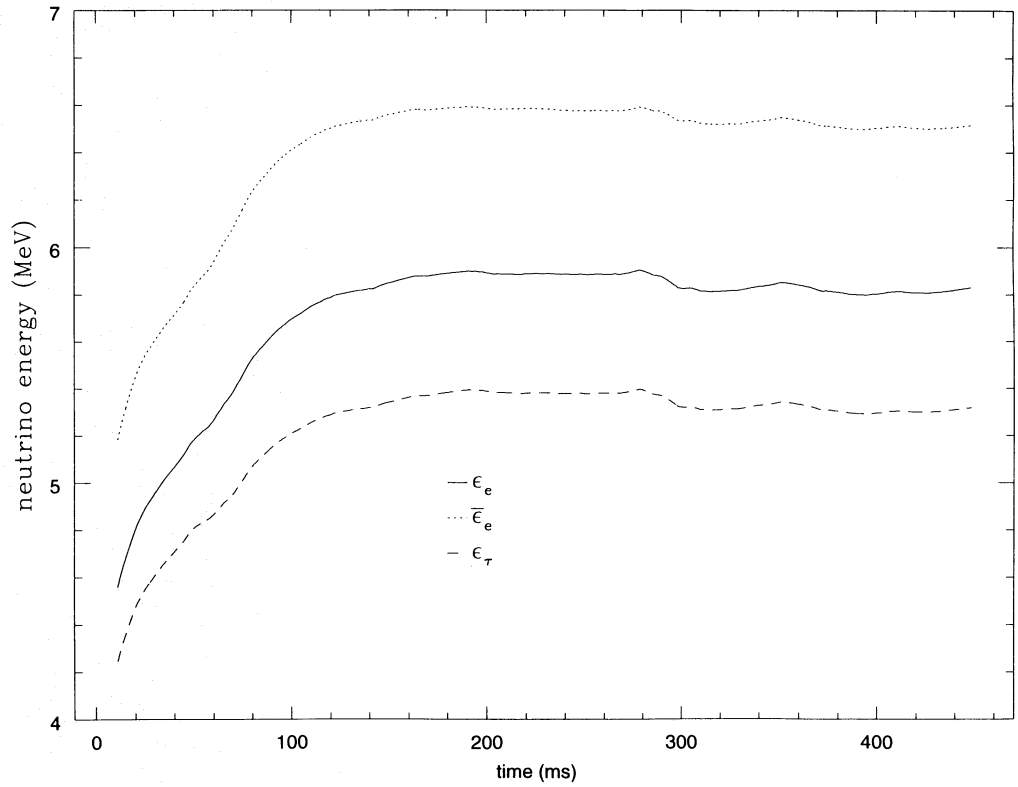

FIG. 12*b*

FIG. 12.—(*a*) Neutrino luminosity and (*b*) mean neutrino energy as a function of time for an $S_{tot} = 80$ equilibrium atmosphere

neutron star. Note that for these high-entropy atmospheres, no entropy "bump" develops through neutrino heating. Figure 13 shows the neutrino luminosities and mean energies vs. time. The neutrino luminosity increases initially and then stabilizes, indicating a constant rate of accretion for the duration of the simulation. In essence, the system has reached a steady state in which the neutrino emission exactly balances the compression work done by gravity on the gas settling on the neutron star. In these conditions, hypercritical accretion is maintained until the neutron star collapses into a black hole.

For each simulation, the constancy of the accretion rate was verified by fitting the accreted mass vs. time with a straight line (see Fig. 14 for a typical fit), and the rms deviation was estimated. Figure 15 presents a comparison between the accretion rate calculated analytically and numerically as a function of atmosphere total entropy. The open symbols were plotted using a straight insertion of the total entropy, while the filled symbols were plotted by computing the radiation entropy from the numerical simulations and using this value in equation (40). The remarkable agreement between analytical and numerical calculations (when the radiation entropy is used) shows that our models are self-consistent. In addition, we note that as entropy increases, the difference between S_{tot} and S_{rad} becomes smaller and smaller. Together with the good agreement with the CHB model, this allows us to extrapolate the behavior of our atmospheres beyond the range of entropies that we have simulated.

Figure 16 shows the analytical accretion rates for high-entropy atmospheres. The lower and upper curves represent the cases with no external pressure, and with external pressure at 1000 km of 0.25% the pressure at the surface of the neutron star, respectively. Of course, in reality the external pressure on the atmosphere is determined by the formation mechanism. However, the limits that we have chosen bound the results from all our infall models (see § 4.1), and it is unlikely that any of the formation mechanisms will produce atmospheres with external pressures beyond these limits. Note also that photons are still trapped out to 100 times the neutron star radius at an entropy $\sim 600\ k_B$ nucleon^{-1}, which is over a factor of 10 times higher than typical stellar entropy values.

4.3. *Summary of Results*

We are now in position to tie together our studies of infall models with the behavior observed in our equilibrium atmosphere simulation, to create a complete picture of the evolution of rapid accretion onto neutron stars (see Table 5). As we know from § 4.2, if the entropy is greater than ~ 600, then the atmosphere is stable over long timescales. For $600 < S < 50$, the atmosphere accretes hypercritically. But for $50 < S < 30$, neutrinos heat the base of the atmosphere, ultimately leading to explosions. The mass accreted before the explosion is $M_{exp} = \dot{M}\tau_{exp}$, where $\dot{M} = (GM_{NS}/r_{NS})/L_\nu$ and $\tau_{exp} \sim \tau_{conv}$. These values are shown in Table 3. The final results for the objects in Table 1 are listed in the last column. Immediate collapse designates atmospheres in the high or intermediate regimes, $S > 600$ atmospheres are stable, $600 < S < 50$ atmospheres suffer delayed collapse, and $50 < S < 30$ atmospheres result in explosions.

We will now summarize these results in terms of accretion rates. Very high rates of infall ($\dot{M} \gtrsim 10^6\ M_\odot\ \mathrm{yr}^{-1}$) clamp the shock close to the neutron star and lead to rapid accretion and black hole formation. Very low rates of infall ($\dot{M} \lesssim 10^{-4}\ M_\odot\ \mathrm{yr}^{-1}$) allow the entropy to rise to about 600

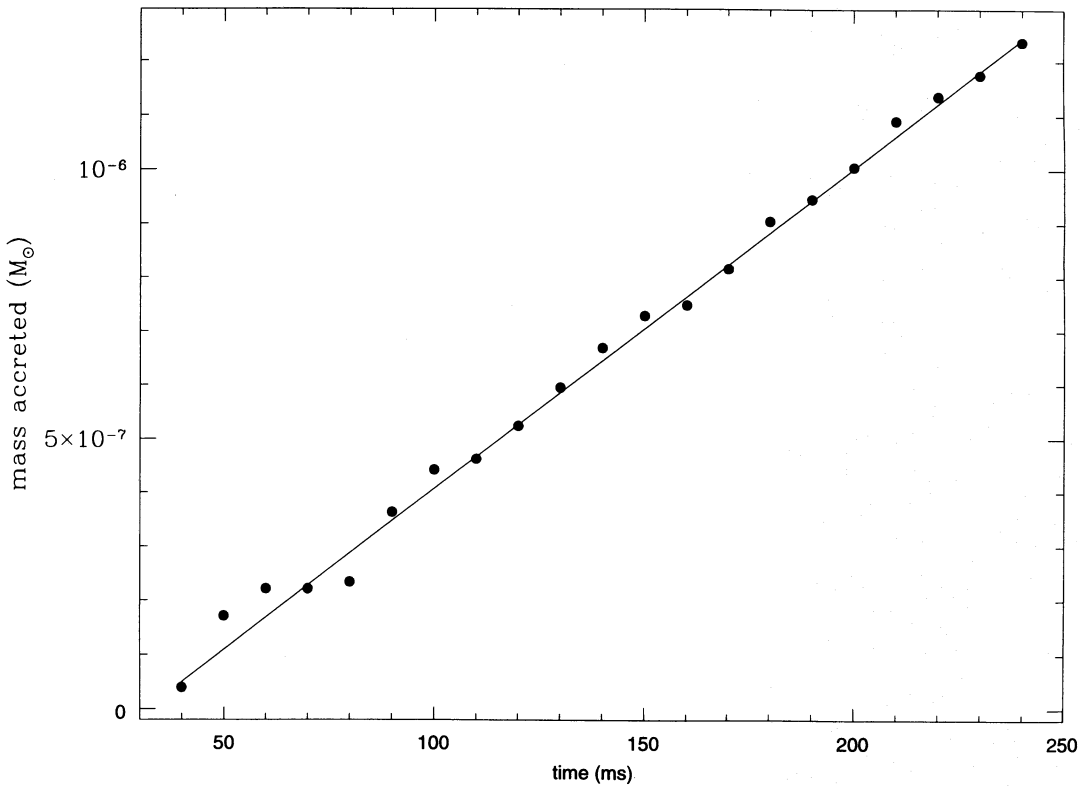

FIG. 13.—Total mass accreted vs. time with the best constant accretion fit for an $S_{tot} = 80$ equilibrium atmosphere

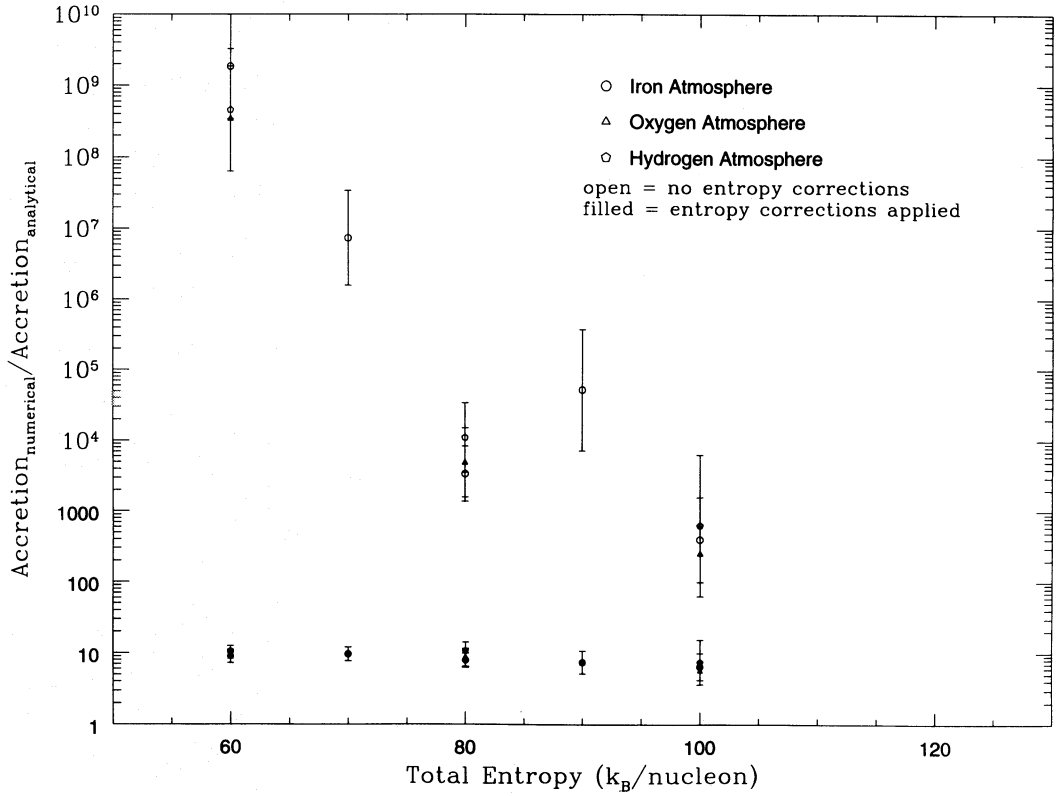

FIG. 14.—A comparison between numerical accretion rates and the analytical results of Colgate et al. (1993). The filled circles compare analytical results using only the radiation entropy from the numerical calculations, whereas the open symbols use the total entropy.

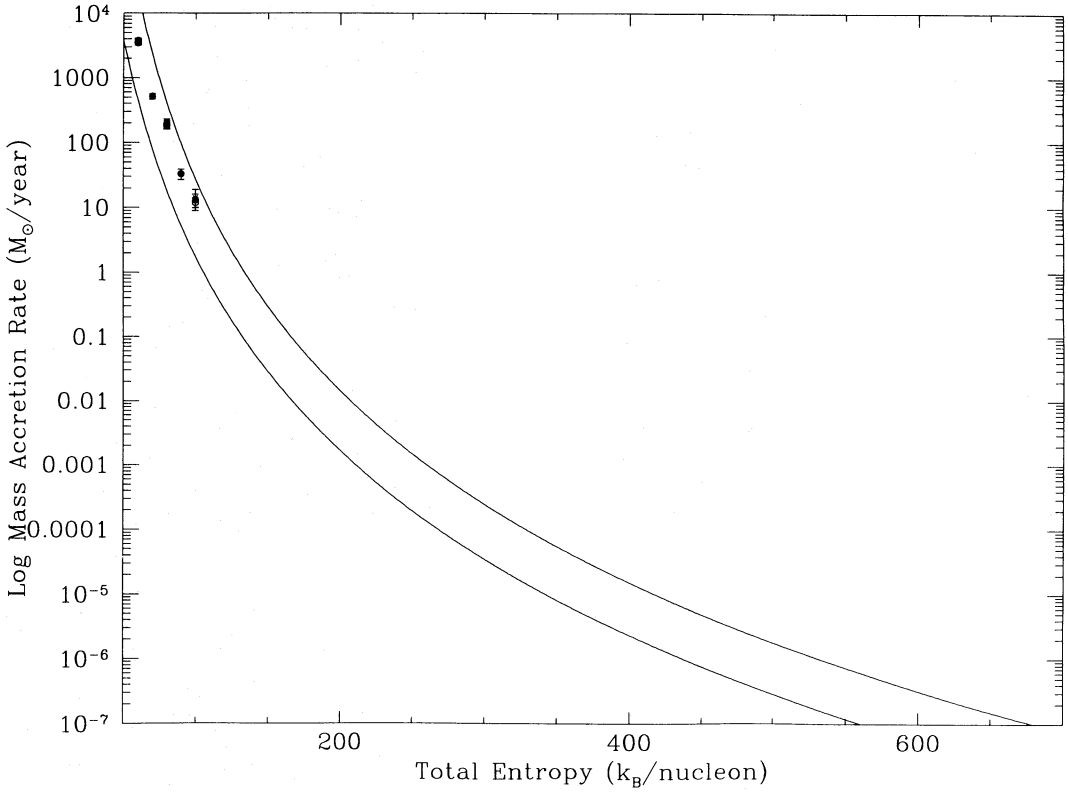

FIG. 15.—Accretion rate vs. entropy. The two lines denote analytical results using outer pressures of 0% and 0.25% that of the pressure at the surface of the neutron star. The points are results from the simulations.

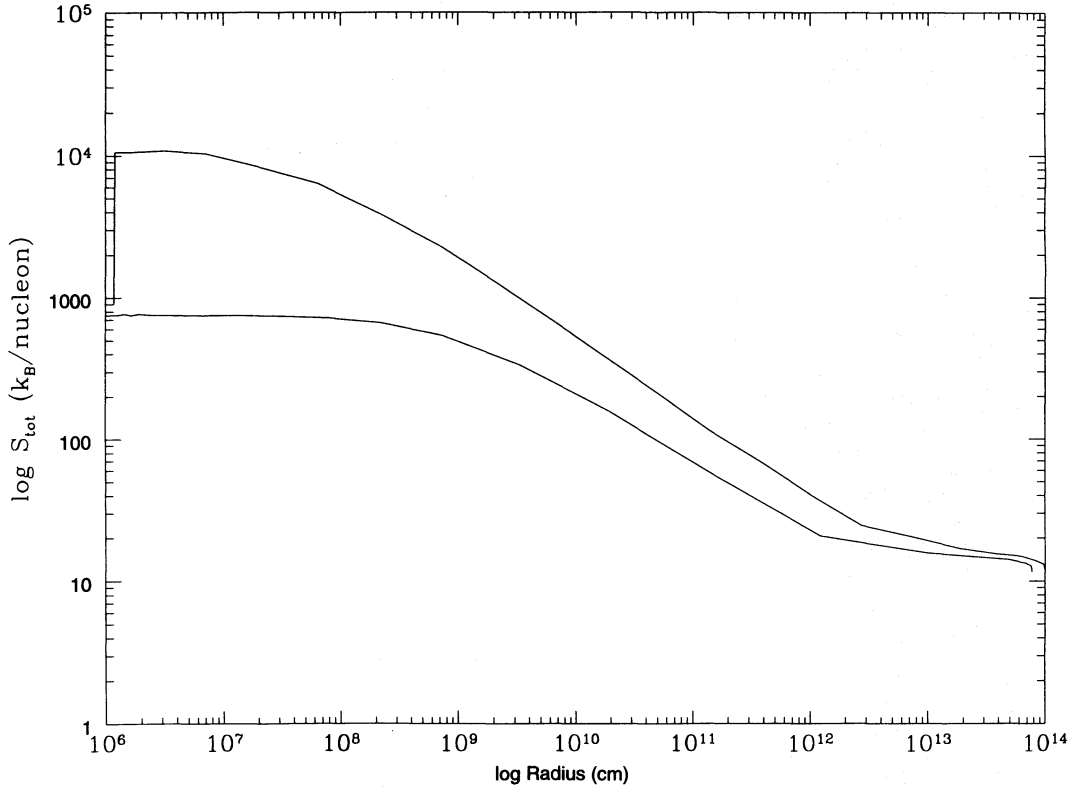

FIG. 16.—Entropy profiles vs. radius for the nucleosynthesis models of Cannon (*top line*) and Biehle (*bottom line*)

k_b nucleon^{-1} and form a stable atmosphere lasting many dynamical times. Low rates ($10^{-4}\ M_\odot\ \mathrm{yr}^{-1} \lesssim \dot{M} \lesssim 0.1\ M_\odot\ \mathrm{yr}^{-1}$) of infall form a stable atmosphere in near pressure equilibrium which nonetheless accretes hypercritically and lead to the eventual formation of a black hole. Medium and low ($0.1\ M_\odot\ \mathrm{yr}^{-1} \lesssim \dot{M} \lesssim 10^3\ M_\odot\ \mathrm{yr}^{-1}$) rates of infall also form a stable atmosphere in near pressure equilibrium, but neutrino heating eventually leads to an explosion rather than black hole formation. Finally, an intermediate rate of infall ($10^3\ M_\odot\ \mathrm{yr}^{-1} \lesssim \dot{M}^6\ M_\odot\ \mathrm{yr}^{-1}$) does not have the time to form a proper atmosphere as it rapidly leads to collapse into a black hole.

4.4. *Initial Transient Revisited*

We have implicitly assumed in § 4.3 that the initial transients define the fate of the system. However, if a system evolves into a steady state, this steady state can be maintained as long as any variations in the infall rate are sufficiently slow that the atmosphere can adapt to the changes before vigorous convection develops. The ultimate fate of the system is identical under the steady state solution and the transient solution for all regimes except the medium-low regime, which results in explosions. Thus, we will limit this discussion to the specific cases in which a steady state system evolves and then the infall rate is gradually changed to place it in the medium-low regime. If the steady state is maintained, the boundary between low and medium-low regimes will rise, limiting the range of atmospheres that fall into the medium-low regime. In this section, we will estimate how slow the infall rate must change to maintain the steady state system under various developments of the infall rate and the modifications to the results if a steady state is maintained.

We will consider two possible scenarios in which we begin with a steady state system and then modify the infall rate: a very high initial rate ($\dot{M} \gtrsim 10^3\ M_\odot\ \mathrm{yr}^{-1}$) corresponding to supernova fallback, and a low initial rate ($\dot{M} \lesssim 10^{-4}\ M_\odot\ \mathrm{yr}^{-1}$) corresponding to stellar encounters. For the very high initial rate, a steady state system cannot be formed because the convection timescale is longer than the timescale for the neutron star to accrete sufficient material to become a black hole. For low initial infall rates, a steady state system can form and be maintained with a sufficiently slow increase in the infall rate.

As we increase the infall rate on an initial equilibrium atmosphere, the entropy of the material at the shock radius

TABLE 5

INFALL RESULTS

Infall Rate	Transient Convection	Neutrino Convection	End Result
$\dot{M} > 10^6\ M_\odot\ \mathrm{yr}^{-1}$	No	No	Black Hole
$10^6\ M_\odot\ \mathrm{yr}^{-1} > \dot{M} > 10^3\ M_\odot\ \mathrm{yr}^{-1}$	No[a]	No	Black Hole
$10^3\ M_\odot\ \mathrm{yr}^{-1} > \dot{M} > 0.1\ M_\odot\ \mathrm{yr}^{-1}$	Yes	Yes	Explosion
$0.1\ M_\odot\ \mathrm{yr}^{-1} > \dot{M} > 10^{-4}\ M_\odot\ \mathrm{yr}^{-1}$	Yes	No	Steady Accretion

[a] A transient is produced, but a black hole forms before it can fully develop.

decreases, becoming lower than the entropy of the equilibrium atmosphere. This system is then unstable to convection. If convection can equilibrate this disparity in entropy before the entropy changes sufficiently to cause vigorous convection, then the system will remain in steady state. We can estimate a minimum timescale required for the convection from our calculation of the convective turnover timescale (see eq. [32]). This timescale was derived assuming the same vigorous convection which we are trying to avoid and is, therefore, certainly an underestimate of the time required. At a radius of 10^{11} cm, the vigorous convective timescale is 1.6×10^4 s. We will discuss the details of convection in the Appendix from which we determine that for density enhancements greater than $\sim 20\%$, the convective velocity rises within a factor of 2 of the sound speed, which is too fast to model under the mixing-length algorithm. We will define "vigorous" convection to begin where mixing length fails. With this approximation and using equation (13), we notice that only for situations in which $\dot{M}$ changes by less than 20% over the convective timescale can a steady state system be maintained. From Table 1, we see that even this underestimate of the timescale precludes most collision formation scenarios, but it allows for the possibility to maintain a steady state in common envelope systems.

As mentioned in § 4.3, for $50 < S < 30$ atmospheres, neutrino heating leads to an explosion. Assuming that the initial transient defines the entropy profile, these entropies are achieved for $\dot{M} \gtrsim 0.1\ M_\odot\ \mathrm{yr}^{-1}$. In the steady state solution, we can use equation (29) and equations (26)–(28) to determine the infall rate above which the equilibrium atmosphere entropy is less than 50: $\dot{M}_{\mathrm{crit}} = 20\ M_\odot\ \mathrm{yr}^{-1}$. Thus, if a steady state is maintained, the critical infall rate between the low (hypercritical accretion) regime and the medium-low (explosion) regime will move from $0.1\ M_\odot\ \mathrm{yr}^{-1}$ to $20\ M_\odot\ \mathrm{yr}^{-1}$.

5. IMPLICATIONS

We can now apply the results from the two sets of simulations to a range of astrophysical situations involving high infall rates onto neutron stars. In this section, we discuss neutron star accretion in the context of TZ objects, common envelope systems, neutron stars in dense molecular clouds, and supernovae. Because our two-dimensional simulations invalidate a number of results previously obtained in one dimension, we present a criterion for the appropriateness of the mixing-length algorithm to model convection. Further, the discussion of specific systems provides examples of the methodology in applying our results to the study of other objects. We end this work with a brief discussion of the observational properties of the explosion regime and a note on plans for future work.

5.1. *TZ Objects*

All the formation scenarios for TZ objects discussed previously (see § 1) involve a neutron star spiralling into a red giant star. As it approaches the core, the infall rate becomes high. For example, a neutron star moving at 100 km s^{-1} at a radius of 5×10^{10} cm inside a 20 $M_\odot$ giant has a mass infall rate of $1.8 \times 10^6\ M_\odot\ \mathrm{yr}^{-1}$. We can easily verify that all our assumptions hold. That is, the time delay due to angular momentum transport is short (~ 0.5 s), and the impact of rotational support is minimal (see § 3.3.2), magnetic fields $\lesssim 10^{15}$ G will be buried by the inflow of material (see §3.3.4), and photons will be trapped out to the Bondi accretion radius (see § 3.3.3). Looking at Tables 3 and 4, we see that this infall fits into the intermediate regime, which forms a shocked atmosphere but accretes it through neutrino emission before it can become completely mixed. These kinds of systems collapse quickly into black holes (for our specific case, the timescale for collapse ~ 1 minute). Hence, the current range of scenarios cited in the literature as possible birth mechanisms for TZ objects will *not* form TZ objects.

Even assuming that a proper formation scenario can be found, it is difficult to imagine how a TZ object could exist for an extended period of time. Peculiarities in the structure of TZO seem to inevitably lead to instabilities which destroy the object. All stellar structure models of TZO have to smoothly connect the base of the envelope to the surface of the neutron star. In order to prevent significant neutrino emission, the base of the atmosphere must remain relatively cool ($\lesssim 10^9$ K). Eich et al. (1989) were able to construct such cool inner regions (which they call insulating layers) with low neutrino emission while maintaining the appropriate pressures. They argued that high-temperature atmospheres would emit neutrinos and turn into the low-temperature stable atmospheres that they had created. Our results clearly show that this is not the case and that once it begins, neutrino emission increases to a high value which maintains a high rate of accretion. In our simulations, after an initial transient, the neutrino emission rate becomes nearly constant (see Fig. 13) rather than shutting itself off after cooling the material at the surface of the neutron star.

This can readily be explained by the fact that energy losses due to neutrinos deleptonize and decrease the specific internal energy of the base of the atmosphere. Since the pressure is set by the structure above, the base of the atmosphere can only adjust and try to maintain pressure equilibrium by compression. This increases density *and temperature* (or if degeneracy has set in, the Fermi energy increases) and thus keeps up the neutrino emission rate until the material is incorporated into the neutron star. It may appear paradoxical that a loss of energy via neutrino emission could increase the temperature (or the Fermi energy). However, we all know that as a star evolves, the entropy of the core continually decreases, while the central temperature keeps increasing (see also eq. [38]). All this is related to the fact that under certain conditions, the heat capacity of gravitational systems can be negative (inasmuch as a gravitational system can be considered a thermodynamical system). As a result, once neutrino emission begins to have a dynamical effect, i.e., the compression of the base of the atmosphere, it will continue to be important. Thus, the low-temperature atmospheres constructed by Eich et al. (1989) are unstable.

In addition, the region above the inner layer postulated by Eich et al. (1989) has to have a high entropy $S > 600$ k_{B} nucleon^{-1}, so that neutrino losses remain unimportant (Fig. 14). Notwithstanding the fact that such entropies are an order of magnitude greater than those found in main-sequence or even giant stars, a gravitational bound atmosphere with $S > 600$ would have little mass (recall Fig. 8). Biehle (1991, 1994), Cannon et al. (1992), and Cannon (1993) have attempted to overcome this mass problem by placing a low-entropy inner region, with associated large negative entropy gradients (see Fig. 16). These atmospheres are, of course, unstable, and Biehle and Cannon use the convective instability to transport energy outward and bring fuel down

into the burning region of their stellar models. However, they treat convection with the mixing-length approximation. While Biehle and Cannon were able to maintain the structure of their atmospheres by assuming mixing-length convection, we have found that this assumption is invalid by running two-dimensional calculations. Figure 17 illustrates the vigorous convection arising from Biehle's initial structure after 0.1 s. This convection eventually drives a shock through the atmosphere, disrupting it and blowing it away.

An intrinsic assumption of mixing-length theory is that the convective evolution is nearly adiabatic, and slow compared to the dynamical timescale so that the evolution can be represented by a series of quasi-static equilibria. As a result, a necessary (but probably not sufficient) criterion for the validity of mixing length is that the sound travel time across a convective cell is much less than the rise time for that cell to move one cell length, or equivalently that the convective velocity is very subsonic. The mathematical details of this criterion are discussed in the Appendix. Table 6 lists the rise times and velocities calculated with equations (A5) and (A6) for the convective cells after they travel one scale height for a typical supernovae simulation, the Sun, and the TZ models of Biehle and Cannon. Note that only for the Sun is the ratio of the rise time over the sound crossing time *much* less than one. Of our four examples, only the Sun satisfies this essential assumption of mixing-length theory.

We have argued above that currently envisioned astrophysical scenarios are incapable of forming TZ objects. It also appears that present models of TZ structures improperly account for convection using the mixing-length algorithm, and thus they result in unphysical objects which are artificially stable.

5.2. *Common Envelope Systems*

For a common envelope system, comparison to our results is less straightforward. Let us again discuss the characteristics of a specific case from Table 1. For a neutron star 10^{12} cm from the center of a 20 $M_\odot$ giant, moving at v_{orb} = 100 km s^{-1}, the infall rate is 175 $M_\odot$ yr^{-1}. Again, photons are trapped out to the Bondi radius and magnetic fields $\lesssim 4 \times 10^{13}$ G will be smothered by the infalling material. Angular momentum induces a significant delay time in the accretion of order 200 s which is nevertheless much less than the orbital timescale. As we shall see, this situation leads to a neutrino-induced explosion.

The convection timescale for this particular case is much less than the neutrino cooling timescale (see Table 4). This corresponds to the medium-low infall rate regime from our

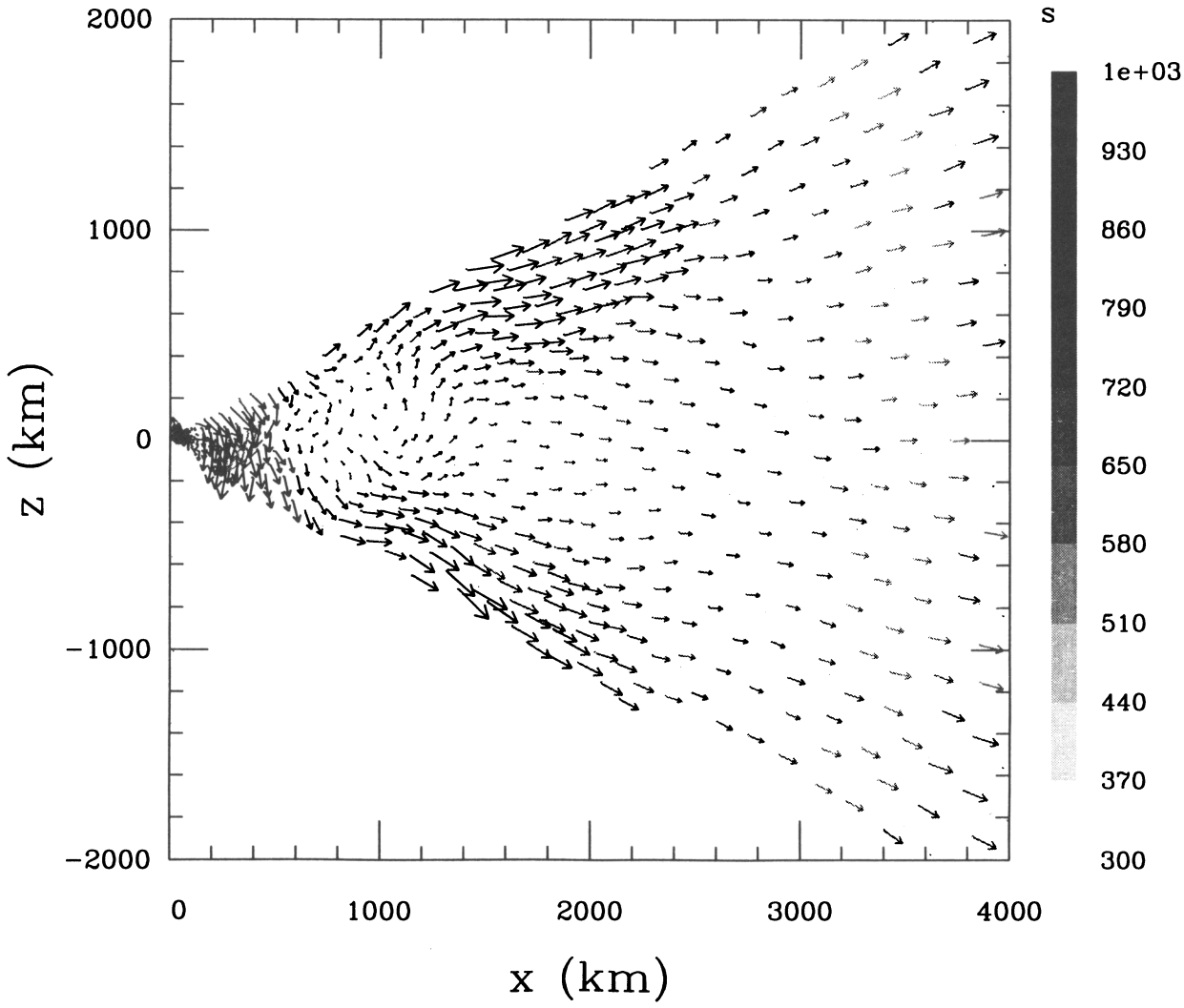

FIG. 17.—Biehle's structure model after 0.5 s. The high-entropy material is driving the atmosphere outward. Outward velocities approach 600 km s^{-1}

TABLE 6

CONVECTION

RATIO	SOLAR ENVELOPE	CORE COLLAPSE SUPERNOVA	MODEL	
			Biehle's TZ	Cannon's TZ
t_{co}/t_{cs}.....	$\sim 2 \times 10^3$	~ 1.2	~ 4	~ 2
v/c_s.....	$\sim 4 \times 10^{-3}$	~ 1.0	~ 0.2	~ 0.5

results. In this regime, the postshock entropy of the infalling material is critical to determine the outcome. From Figure 2, it is clear the accretion shock will lie at a radius $> 10^8$ cm, and using equation (29) the postshock entropy will be $\lesssim 50$ k_B nucleon^{-1}, if the shock is strong, which it is not since this value is close to the specific entropy of the material outside the Bondi radius. Nevertheless, this allows us to estimate that the entropy of the equilibrium atmosphere which forms above the neutron star corresponds to $29 < S < 50$, where the upper limit comes from the maximum post accretion shock entropy and the minimum comes from the entropy of the ambient matter.

From our models of equilibrium atmospheres (see § 4.2), we know that these conditions will lead to explosions. These explosions may be sufficient to blow off the atmosphere and halt the inward spiral of the neutron star, forming close binary systems such as PSR 1913+16 (see Smarr & Blandford 1976 or Burrows & Woosley 1986). However, if the injected energy is insufficient to completely expel the atmosphere, the neutron star continues to fall into the giant star, as a new atmosphere once again builds up around it. Extrapolating from Table 4, we estimate that the neutron star might survive 50 outbursts over 100 yr before it accretes ~ 0.2 $M_\odot$. Simulations of double core evolution (Terman et al. 1994) estimate inspiral times $\lesssim 1$ yr with some cases where the energy input from viscous forces on the neutron star ($\sim 10^{47}$ ergs) is sufficient to drive off the envelope and halt the inward spiral of the neutron star. The neutron star will certainly survive this evolution, and this offers yet another way to form close binary systems.

However, we must qualify our claims here. As we have said before, it is not possible to run a continuous simulation from the convective infall regime to the stable equilibrium atmosphere which eventually appears. Thus, we are forced to infer indirectly the entropy of this equilibrium atmosphere from the early behavior observed in our infall simulations. Should the entropy for some reason end up larger than 50, then an explosion will not occur, but rather, the atmosphere will undergo steady, hypercritical accretion until the neutron star collapses to form a black hole.

5.3. *Supernovae*

At present, the details surrounding the explosion mechanism for supernovae are not sufficiently well understood to place any firm constraints on the fallback of matter onto the neutron star after a successful explosion (e.g., see Herant et al. 1994). Taking into account these uncertainties, we would still like to address the questions of whether fallback can lead to the formation of a black hole or a secondary explosion. A 25 $M_\odot$ supernova progenitor exploded by Woosley & Weaver (1995) gives rise to an initial fallback rate of 10^7 $M_\odot$ yr^{-1}, decreasing thereafter. This initial value is just within the high accretion regime which corresponds to unrestricted accretion by the neutron star. This may or may not push the neutron star over its maximum mass and make it collapse into a black hole. If this does not happen, the declining accretion rate will eventually reach the low infall regime which corresponds to explosions. Those would then blow off the remaining bound atmosphere. Note that the infall rate from this particular simulation was near the division between the high and low infall regimes, implying that uncertainties in the explosion mechanism coupled with differences between supernova progenitors may lead to very different outcomes, one in which a black hole forms, and another in which a secondary explosion expels the remaining material bound to the neutron star.

5.4. *Explosions*

Explosions add an entirely new observational dimension to the evolution of rapid mass infall systems which we have considered in this paper. Physically, these explosions are most akin to Type II supernovae, and thus, some of the observational aspects may be similar (velocities, compositions), even though the amount of mass expelled and energy should be a factor of 10^{-5} smaller. Moreover, it is clear that the extent and amount of material in which a neutron star is embedded during an explosion will have a crucial impact on the observational signature. The range of possible signatures is vast, requiring a more detailed analysis which we relegate to future work. However, in some circumstances, these supernova-like objects may still be bright enough to be seen in nearby galaxies.

Using observed abundances of Be systems and massive binary systems, Biehle (1991) has derived the formation rate of common envelope systems to be between 2×10^{-5} and 6×10^{-4} per year in our galaxy. Using the entire set of observations of massive X-ray binaries, Cannon (1993) gave a not too different estimate of 10^{-3} objects per year in our galaxy. Iben, Tutukov, & Yungelson (1996) predict 1.5×10^{-3} objects using an entire neutron star census. Because the "embedding" companion star will usually be massive, explosions in these systems are likely to be damped as they propagate through the massive envelope. Therefore, they may appear only as enhancements of an already strong wind and changes in chemical abundances.

Focusing on globular clusters, Davies & Benz (1995), have obtained a reliable formation rate of 10^{-8} per year per cluster (which corresponds to $\sim 10^{-6}$ per year per galaxy) through extensive encounter simulations. They also predict that these collisions generally result in an ~ 0.3 $M_\odot$ atmosphere remaining bound to the neutron star. Owing to the smaller amount of mass surrounding the neutron star, explosions from these atmospheres will be less damped and might be observed as supernova-like objects. However, the low formation rates limit the observational prospects for these objects. One should note, though, that these objects have been proposed as progenitors of millisecond pulsars. If, instead, they blow off their atmospheres before accreting

sufficiently to be spun up, other scenarios for the production of millisecond pulsars will have to be found. Further study including angular momentum effects will better address this problem. Similarly to globular clusters, as dense stellar systems, galactic bulges offer opportunities for mergers involving neutron star through collisions. However, we are not aware of reliable estimates for collisional rates in the galactic center.

Leonard et al. (1994) investigated the scenario in which the velocity kick received by a neutron star in a supernova explosion makes it merge with a binary companion. They predicted an occurence rate of 2.5×10^{-4} per year in our Galaxy. These systems may result in an inward spiraling neutron star. However, since the kick produces collisions with similar velocities to those from the globular cluster collisions of Davies & Benz, we might instead expect the likely result to be $\sim 0.3\ M_{\odot}$ smothered neutron stars as predicted in their models. Assuming the latter to be the case, we would expect 1% of observed supernovae to produce a secondary explosion and lead to a peculiar structure of the remnant.

5.5. *Future Work*

We would like to follow up the discovery of these "accretion-induced" explosions with detailed calculations of their observable signatures. The observational prospects for the ejection of neutron star atmospheres are tightly linked to the fraction of encounters which result in energetic explosions. This fraction is in turn strongly dependent on the effects of angular momentum. While at best difficult, accounting for those effects will be essential to understanding neutron stars accreting at high rates. We would also like to determine the observational properties and chemical composition of the ejected material. This will be addressed in future work.

Although it is an interesting topic, we have not discussed the case of neutron star embedded in dense molecular clouds or in AGN disks elsewhere in this paper. Unfortunately, in these conditions, the photon trapping radius is within the Bondi radius so that radiation transport plays an important role in the evolution. It is plausible that the dense molecular cloud will first accrete slowly, at the Eddington rate, until sufficiently high pressures and temperatures near the neutron star surface develop, leading then to hypercritical accretion or possibly an expulsion of the material. This ejecta will enrich the surrounding medium and, since the mass accretion will be low, may be a repeatable process, facilitating an important mechanism to enrich the interstellar medium or the disk of an AGN. Understanding these effects will require the implementation of a radiation transport scheme.

This paper has benefited from the contributions of many people. We are grateful to Raph Hix for making available his nuclear statistical equilibrium code, to Doug Swesty for his nuclear equations of state, to Dimitrij Nadezhin for his equation of state, and to Chuck Wingate for his graphics software. We thank Dave Arnett for use of his stellar structure code and many helpful discussions. Stirling Colgate for his advice and for bringing up many of the questions motivating this paper, and Stan Woosley for his supernova fallback scenario and related discussions. Discussions with Grant Bazan, Adam Burrows, Roger Chevalier, Melvyn Davies, and Doug Lin have also served to clarify aspects of this paper. The work of C. F. and W. B. was partially supported by NSF grant AST 9206738 and a "Profil 2" grant from the Swiss National Science Foundation. The work of M. H. was supported by a *Compton Gamma Ray Observatory* postdoctoral fellowship at the University of California, Santa Cruz, and by a director's postdoctoral fellowship at the Los Alamos National Laboratory.

APPENDIX

A NECESSARY CRITERION FOR THE VALIDITY OF THE MIXING-LENGTH APPROXIMATION FOR CONVECTION

Despite the many problems with mixing length (choice of scale height, etc.), there is no better convection algorithm short of multidimensional simulations. Hence, mixing-length theory remains the most common technique for dealing with convective instabilities. It is thus worthwhile to try to derive a simple criterion to verify the validity of a mixing-length approach in a given situation. An intrinsic assumption of mixing-length theory is that the convective evolution is nearly adiabatic, and slow compared to the dynamical timescale so that the evolution can be represented by a series of quasi-static equilbria. As a result, a necessary (but probably not sufficient) criterion for the validity of mixing length is that the sound travel time across a convective cell is *much* less than the rise time for that cell to move one cell length, or equivalently that the convective velocity is very subsonic. In the following paragraphs, we first provide a rigorous calculation of the motion of a convective cell, which we then complement with a more physically intuitive interpretation. We go on to show that typical convective neutron star atmospheres do not satisfy our criterion and therefore cannot be modeled using mixing length.

The sound travel time across a cell is simply given by

$$\tau_s = H_p / c_s \,, \tag{A1}$$

where H_p is the convective scale length, typically approximated as the pressure scale height, and c_s is the sound speed of the convective cell. The acceleration for the cell is (see Hansen & Kawaler 1994 for a basic summary)

$$a_{\rm cell} = a_{\rm buo} + a_{\rm vis} = g\left(1 - \frac{\rho}{\rho_c}\right) - \frac{\eta}{\rho}\nabla^2 v - \frac{\theta_{\rm turb}}{V\rho} \,, \tag{A2}$$

where g is the gravitational acceleration at the position of the cell, ρ_c is the density of the cell, ρ is the density of the medium

through which the cell is passing, and V is the volume of the cell. The quantity η is the linear viscous term and can be written (see Kippenhahn & Weigert 1990)

$$\eta \approx \eta_{\rm th} + \eta_{\rm rad} \approx \rho l_{\rm mfp} v_{\rm th} + aT^4/c\kappa\rho \ , \tag{A3}$$

where $l_{\rm mfp}$ is the electron mean free path and $v_{\rm th}$ is the electron's thermal velocity. We shall approximate $\nabla^2 = v/(fH_p)^2$, where $f < 1$ (in our calculations, we choose $f = 0.01$). The term $\theta_{\rm turb}$ is the turbulent drag (see, for example, Shames 1992):

$$\theta_{\rm turb} \approx \frac{C_{\rm turb}\,\rho v^2 A}{2} \ , \tag{A4}$$

where $C_{\rm turb}$ depends upon how streamlined our convective cells are (values range from 0.01–1, and we conservatively use 1), and A is the effective surface area of the cell.

We can then integrate this equation to determine the velocity of the cell (assuming it starts at rest) and distance as a function of time:

$$v = (L + M)\left\{(e^{2Lct} - 1)\Big/\left[\left(\frac{L + M}{L - M}\right)e^{2Lct} + 1\right]\right\} , \tag{A5}$$

$$x = -\ln\left\{\left[\left(\frac{L + M}{L - M}\right)e^{2Lct} + 1\right]\Big/c\right\} - (L + M)t + \ln\left\{\left[\left(\frac{L + M}{L - M}\right) + 1\right]\Big/c\right\} , \tag{A6}$$

where $L = [b^2/(4c^2) - a/c]^{1/2}$ and $M = b/2c$ with $a = a_{\rm buo}$, $b = -\eta/(f\rho H_p^2)$, and $c = -(C_{\rm turb}\,\rho A)/(2\rho_c)$. Setting $x = H_p$, one can solve for the rising timescale and determine whether the solution can be appropriately modeled with a mixing-length algorithm.

In most circumstances, the dominant viscous force arises from the turbulent drag term. Ignoring the linear viscous terms simplifies the preceding equations and provides a more intuitive picture of the conditions required for using the mixing-length formalism (although we recommend the general argument for any applications). As we stated earlier, a necessary condition for mixing length is that the sound travel time is much less than the convective travel time, or equivalently, the convective velocity must be much slower than the sound speed. By eliminating the linear term from equation (A2), using equation (A4) with $A/V = 1/H_p$, and setting $g = \nabla P/\rho = P/(\rho H_p)$, we can solve for the maximum bubble velocity:

$$v_{\rm max} = \sqrt{\frac{2P}{\rho C_{\rm turb}}\left(\frac{\rho}{\rho_c} - 1\right)} = c_s\sqrt{\frac{2}{C_{\rm turb}\,\gamma}\left(\frac{\rho}{\rho_c} - 1\right)} . \tag{A7}$$

For a $\gamma = 4/3$ gas and $\rho_c < 0.85\rho$, we find that $v_{\rm max} > 0.5c_s$, violating the mixing-length assumption that $v \ll c_s$. However, these high velocities are only a problem if the bubble can attain them before dispersing. We can estimate the velocity of the bubble after traveling a distance d by assuming that the turbulent viscosity is small until v approaches $v_{\rm max}$:

$$v = \sqrt{2da} = c_s\sqrt{\frac{d}{H_p}\frac{2}{C_{\rm turb}\,\gamma}\left(\frac{\rho}{\rho_c} - 1\right)} . \tag{A8}$$

Setting $d = H_p$ gives $v \to v_{\rm max}$. It is likely, then, that the bubble will approach its maximum velocity after rising one scale length. The ratio of the bubble density to the density of the ambient medium is clearly the primary parameter behind this necessary criterion for mixing length and can be simply applied to any system. One merely needs to determine the buoyancy (or density) of a bubble raised adiabatically one scale height.

REFERENCES

Benz, W. 1991, in Late States of Stellar Evolution and Computational Methods in Astrophysical Hydrodynamics, ed. C. B. de Loore (Berlin: Springer), 259
Benz, W., & Hills, J. G. 1992, ApJ, 389, 546
Biehle, G. T. 1991, ApJ, 380, 167
———. 1994, ApJ, 420, 364
Bisnovatyi-Kogan, G. S., & Lamzin, S. A. 1984, Soviet Astron., 28, 187
Blinnikov, S. I., Dunina-Barkovaskaya N. V., & Nadezhin, D. K. 1995, A&A, submitted
Bondi, H. 1952, MNRAS, 112, 195
Brown, G. E. 1995, ApJ, 440, 270
Burrows, A., & Woosley, S. 1986, ApJ, 308, 680
Cannon, R. C. 1993, MNRAS, 263, 817
Cannon, R. C., Eggleton, P. P., Zytkow, A. N., & Podsiadlowski, P. 1992, ApJ, 386, 206
Chevalier, R. A. 1989, ApJ, 346, 847 (C89)
———. 1993, ApJ, 411, L33
———. 1995, ApJ, submitted
Colgate, S. A. 1971, ApJ, 163, 221
Colgate, S. A., Herant, M., & Benz, W. 1993, Phys. Rep., 227, 157 (CHB)
Cox, A. N., Vauclair, S., & Zahn, J. P. 1983, Astrophysical Processes in Upper Main Sequence Stars (CH-1290 Sauverny: Geneva Observatory)
Davies, R. E., & Pringle, J. 1980, MNRAS, 191, 599
Davies, M. B., & Benz, W. 1995, MNRAS, submitted
Gamow, G. 1937, Structure of Atomic Nuclei and Nuclear Transformations (Oxford: Oxford Univ. Press)
Eich, C., Zimmerman, M. E., Thorne, K. S., & Zytkow, A. N. 1989, ApJ, 346, 277
Frail, D. A., Gross, W. M., & Whiteoak, J. B. Z. 1994, ApJ, 437, 781
Fryxell, B. A., & Taam, R. E. 1988, ApJ, 335, 862
Hansen, C. J., & Kawaler, S. D. 1994, Stellar Interiors-Physical Principles, Structure, and Evolution (New York: Springer Verlag)
Herant, M., Benz, W., Hix, W. R., Fryer, C. L., & Colgate, S. A. 1994, ApJ, 435, 339 (HBHFC)
Herant, M., & Benz, W. 1992, ApJ, 387, 294
Herant, M., Benz, W., & Colgate, S. A. 1992, ApJ, 395, 642
Hix, R., Thielemann, F. K., Fushiki, I., & Truran, J. W. 1995, in preparation
Iben, I., Tutukov, A. V., & Yungelson, L. R. 1996, 456, 750
Houck, J. C., & Chevalier, R. A. 1991, ApJ, 376, 234 (HC)
Kippenhahn, R., & Weigert, A. 1990, Stellar Structure and Evolution (Berlin: Springer-Verlag)
Landau, L. D. 1937, Dokl. Akad. Nauk SSSR, 17, 301
Lattimer, J. M., & Swesty, F. D. 1991, Nucl. Phys. A, 535, 331
Leonard, P. J., Hills, J. G., & Dewey, R. J. 1994, ApJ, 423, L19
Lyne, A. G., & Lorimer, D. R. 1994, Nature, 369, 127
Nadezhin, D. K. 1974, Naucnye Informatsii Astron. Soviet Akad. Nauk SSSR, 32, 33

Ruffert, M. 1994a, ApJ, 427, 342
———. 1994b, A&AS, 106, 505
———. 1995, ApJ, submitted
Ruffert, M., & Anzer, U. 1995, A&A, 295, 108
Ruffert, M., & Arnett, W. D. 1994, ApJ, 427, 351
Sawada, K., Matsuda, T., Anzer, U., Börner, H., & Livio, M. 1989, A&A, 221, 263
Smarr, L. L., & Blandford, R. 1976, ApJ, 207, 574
Shames, I. H. 1992, Mechanics of Fluids (New York: McGraw-Hill)
Shapiro, S. L., & Teukolsky, S. A. 1983, Black Holes, White Dwarfs, and Neutron Stars (New York: Wiley)
Taam, R. E., Bodenheimer, P., & Ostriker, J. P. 1978, ApJ, 222, 269
Taam, R. E., & Fryxell, B. A. 1989, ApJ, 339, 297
Terman, J. L., Taam, R. E., & Hernquist, L. 1994, ApJ, 422, 729
Theuns, T., & Jorissen, A. 1993, MNRAS, 265, 946
Thorne, K. S., & Zytkow, A. N. 1975, ApJ, 199, L19
———. 1977, ApJ, 212, 832
Van Riper, K. A. 1979, ApJ, 232, 558
———. 1995, ApJS, 101, 181
Zeldovich, Ya. B., Ivanova, L. N., & Nadezhin, D. K. 1972, Soviet Astron.-AJ, 16, 209